Simulation of the electron and ion movement through a 4-GEM stack

Master's Thesis
by
Misbah Uddin Ahmed

First examiner: Prof. Dr. Harald Appelshäuser
Second examiner: Dr. Jens Wiechula

Abstract

The ALICE Time Projection Chamber (TPC), the main tracking device in the ALICE central barrel, will undergo a remarkable upgrade before RUN 3 (2021 to 2023). The previous TPC readout chamber is based on Multi-Wire Proportional Chambers (MWPCs). It has been replaced by a new Gas Electron Multiplier (GEM) technology during LS2(2019-2020). Unlike MWPCs, GEM-based technology offers an intrinsic ion suppression which allows the TPC to operate in an ungated and continuous readout mode. The front-end electronics also went through an upgrade to achieve the continuous readout scheme. The new readout chamber consists of a stack of four GEM foils with different hole geometry. The main motivation of this thesis is to analyze the electron and ion movements through a 4-GEM stack. Simulation is carried out for each GEM foil of the stack separately with Garfield++, ANSYS, and Magboltz. The electron and ion transport parameters are defined and formulas are formed to obtain the number of extracted electrons and ions from each GEM foil. Later, the transport parameters such as total effective gain, IBF, epsilon of the 4-GEM stack are calculated using the formulas. The simulation is also adjusted in order to resemble previous measurements and simulations so that the data can be compared for an in-depth understanding. Several attempts were made to optimize the simulation data by changing the GEM geometry and gas properties. Although the simulation describes the changing patterns of the transport parameters for single GEM foils, the combined results for the 4-GEM stack do not reproduce the results of previous measurements. The limitations of the simulation are also discussed in the thesis.

Contents

Chapter 1

ALICE detector system

ALICE (A Large Ion Collider Experiment) is an experiment dedicated to studying heavy ion physics. It is one of the eight experiments at the LHC (Large Hadron Collider) at CERN. It focuses on studying strongly interacting matter at extremely high energy densities and temperatures where the QGP phase is created. The results obtained from ALICE, in particular, are used to understand color confinement, restoration of chiral-symmetry, and the evolution of QGP to hadronic matter [1].

The ALICE detectors can be divided into three categories according to their position, range, and functionality. They are designed to identify particles such as hadrons, electrons and photons. Detectors in the central barrel section provide a full 360° azimuthal coverage and $|\eta| < 0.9$ pseudorapidity acceptance. Central single-arm detectors cover a smaller range than the previously mentioned section. For instance, the High Momentum Particle Identification Detector (HMPID) gives a pseudorapidity coverage of $|\eta| < 0.6$ and azimuthal coverage of 1.2°< ϕ <58.8° [2]. Detectors in the forward region are also designed to manage a large area coverage. For example, the Photon Multiplicity Detector has a 360° azimuthal coverage and pseudorapidity acceptance range. The names of the detectors are listed in Table 1.1 according to their categories.

Category	Name of the detectors
Central barrel	The Inner Tracking System, Time Projection Chamber, The Transition Radiation Detector, The Time Of Flight detector
Central single-arm detectors	The High Momentum Particle Identification detector, The Photon Spectrometer, The Electromagnetic Calorimeter
Forward region	The Di-muon Forward Spectrometer, The Zero Degree Calorimeter, Time0 detector, Vertex0 detector, Forward Multiplicity Detector, the Photon Multiplicity Detector

Table 1.1: Name of the detectors according to their positions in the ALICE.

1.1   The ALICE Time Projection Chamber

The Time Projection Chamber (TPC) is the main tracking device of the ALICE experiment's central barrel. It tracks the charged particles and provides identification by measuring the specific energy loss per track length ($\frac{dE}{dx}$) and particle momentum. In Fig. 1.1, it can be seen that the TPC is situated around the interaction point of the two LHC beams.

The TPC has a hollow cylindrical shape. The whole structure can be separated into two
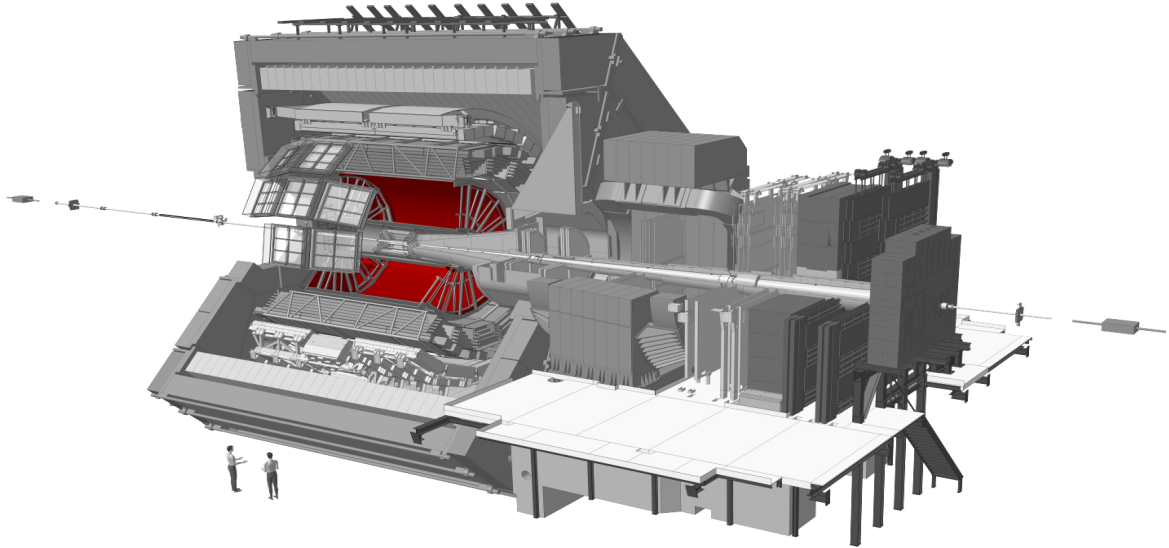
Figure 1.1: The TPC (highlighted in red)inside of the ALICE detector system [3].

components: *field cage* and *readout chambers*. Both components are placed in a tight gas volume with a size of about $88\,\mathrm{m}^3$. The TPC is $5.4\,\mathrm{m}$ long and has a diameter of $5.6\,\mathrm{m}$. Moreover, the *field cage* is divided into two drift regions by the *central electrode* (CE). Each of these drift regions is $250\,\mathrm{cm}$ long. The CE is made of a thin layer of aluminized mylar and is located at the axial center of the cylinder (see Fig. 1.2).
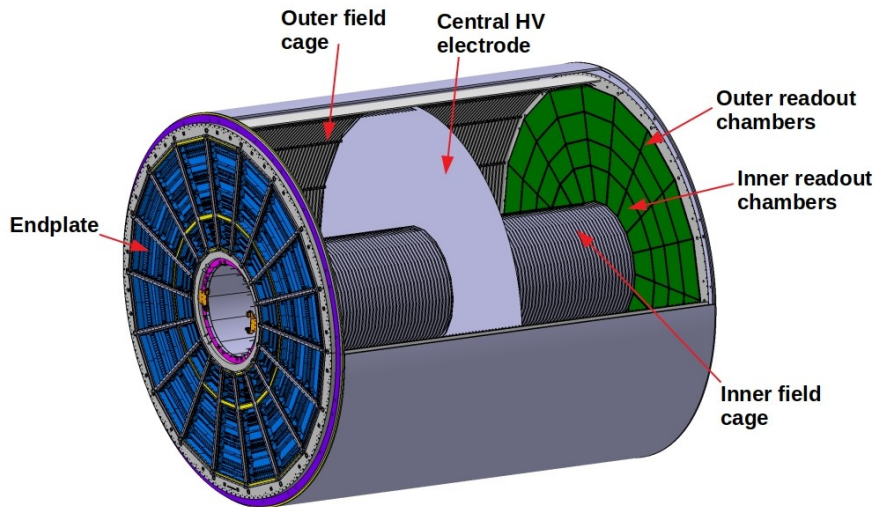

Figure 1.2: Schematic view of the ALICE TPC [4].

Both ends of the TPC are sealed with end-plates where the *readout chambers* are mounted. The *readout chambers* (ROCs) are radially segmented into two types called *inner readout chamber* (IROC) and *outer readout chamber* (OROC). They are positioned in pairs to form 18 equal azimuthal sectors. The technology that the ALICE TPC has adopted for the ROCs in LHC RUN 1 and 2 (2009–2018) is called Multi-Wire Proportional Chamber (MWPC). The MWPC technology has been replaced by new GEM-based technology before LHC RUN 3. The GEM technology will be discussed in detail in Section 1.5.

1.2   Working principle of the ALICE TPC

A charged particle traversing a gas medium makes inelastic collisions with the gas particles along its path, therefore ionizes the gas and produces many electron-ion pairs. The electron-ion pairs are separated by an electric field to prevent them from recombining and to get a signal in the readout chamber. The CE with $100\,\text{kV}$ provides a uniform electric field of $400\,\text{V}\,\text{cm}^{-1}$throughout the entire gas volume. As a result, the produced electrons move towards the readout chamber while the ions drift towards the CE. The TPC is designed for three-dimensional reconstruction of the trace left by the charged particle to identify the particle. As electrons move towards the readout chamber, where the projection of the track is measured with the help of a reconstruction software and tracking algorithm. When an electron reaches the readout chamber, the reconstruction software calculates every 3D space point where it ionized the gas particles. After that, the tracking algorithm connects these space points to make the full particle trajectory. A magnetic field with $0.5\,\text{T}$ is also placed in parallel to the electric field. The particle's rigidity can be obtained from the curvature of the particle trajectory with the help of the magnetic field. Later, the measured energy loss per track length and calculated rigidity combinedly provide sufficient information for particle identification.

1.3   MWPC mechanism

The MWPCs have three wire grid layers: gating grid, cathode wire grid, anode wire grid, and a pad plane (see Fig. 1.3). The gating grid can operate either in open or closed mode, also known as bipolar mode. In the open mode, all the wires are at the same voltage, which allows the electrons to travel towards the amplification region. Open mode is also called transparent mode because the wires are transparent to the charged particles as the gate potential is put to a constant voltage matching this of the ideal drift field. However, the disadvantage of having a permanent open mode is that the gating grid can influence neither the electron traveling from the drift region to the MWPCs nor the ions drifting from the amplification region to the drift region. As a result, unwanted particles also participate in the amplification process, and a field distortion caused by the back drifting ion cloud can be observed.

To avoid this problem the gating grid can operate in closed mode. In this case, an additional bipolar potential is applied which prevents the ions from drifting back to the drift volume. At the same time, on the other hand, it blocks the electrons coming from the detector resulting in a dead time. The dead time causes a rate limitation of the TPC which is in the order of $1\,\text{kHz}$–$3\,\text{kHz}$ depending on the gas mixture [6]. One of the main goals for replacing MWPCs with GEM-based technology is to overcome the dead time and allow for a continuous readout.
After crossing the gating grid, electrons move towards the anode wire grid for amplification. In the amplification, a considerable amount of electron-ion pairs is produced. The produced electrons create an induced signal on the pad plane before ending up on the anode wire within a very small amount of time ($<1\,\mu\text{s}$). Unlike the electrons, produced ions create a larger induced signal on the pad plane, anode wire, and cathode. Nevertheless, only the induced clusters on the pad plane are measured to produce the projection of the particle trajectories.
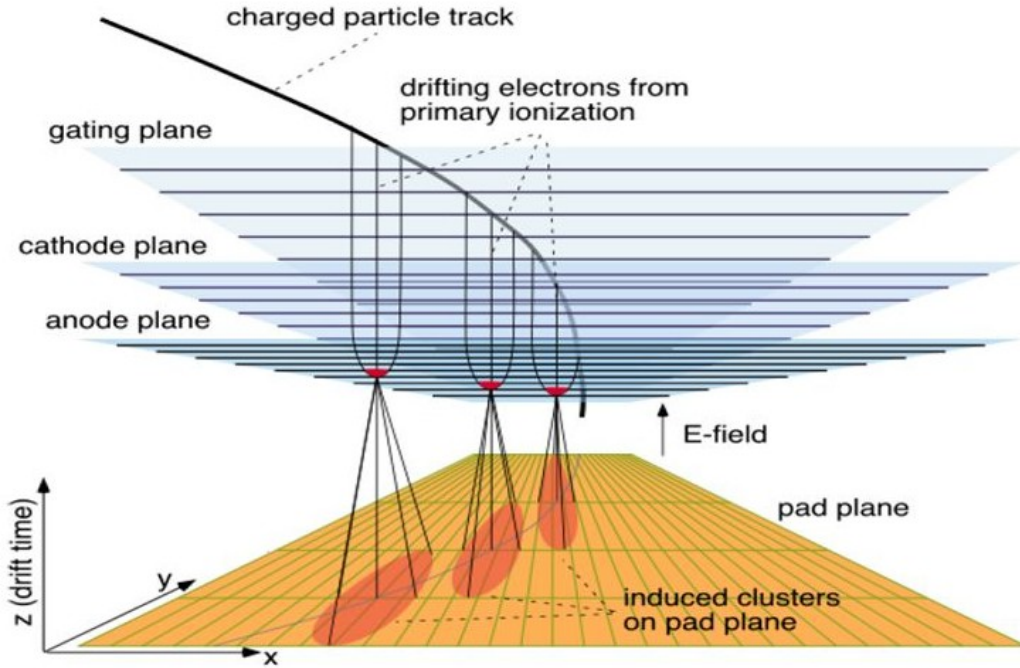
Figure 1.3: An illustration of Multi-Wire Proportional Chamber with pad plane [5].

1.4 Gas choice

Several gas compositions were used in the TPC gas volume in different RUNs. The gas composition has a significant influence on charge movements throughout the drift volume and the amplification process. Hence, selecting the best-suited gas mixture is extremely important. The expected properties of the gas are high ion mobility, high Townsend coefficient, high electron drift velocity, large energy loss, low diffusion coefficient, low attachment coefficient [7]. Electrons follow the field lines in the electric field towards the high potential with mean drift velocity (v_d). The drift velocity is the average velocity gained by a charged particle in material under the influence of an electric field. It also depends on temperature and pressure. It can also be affected by the pollutants such as Oxygen or water molecules mixed with the primary gas. High drift velocity is one of the critical factors in the case of selecting the gas for TPC. The drift velocity equation can be written as:

$$v_d = \mu \mathbf{E} \tag{1.1}$$

$\mathbf{E}$ and μ are called Electric field and electron mobility respectively.
Moreover, electrons deviate from the average field direction because of the gas atoms scattering resulting in longitudinal and transverse diffusion. Thus, gas with a low diffusion coefficient is preferable. After averaging over a large number of collisions, the equation for the diffusion coefficient can be written as:

$$D = \frac{2}{3} \frac{\varepsilon \mu}{e} \tag{1.2}$$

Here, ε is the total energy of an electron.

The mean free path is defined as the average distance an electron passes between ionizing collisions and the inverse of this is the number of ionizing collisions per unit length, also known as the Townsend coefficient. It greatly influences the gas gain. Therefore, a gas with a high Townsend coefficient is preferable for TPC operation. Neon (Ne) and Argon (Ar) based gas mixtures were initially considered as they fulfilled these requirements.

In addition to the electrons, a number of UV photons are produced in the amplification. A fraction of them can be energetic enough to ionize the gas and creating avalanche which could cause a system breakdown. A quench gas is needed to mix with the noble gas to solve that problem. The quencher gas molecules have large photo-absorption coefficients over a wide range of wavelengths. After analyzing properly, CO_2 was selected as the quencher gas among other options such as CF_4. Because of Argon's lower ion mobility, the possibility of larger field distortion caused by back drifting ions is considerably high. In fact, the mobility of Ar^+ ion ($1.52\,cm^2\,V^{-1}\,s^{-1}$) is about three times lower than that of Ne^+ ($4.08\,cm^2\,V^{-1}\,s^{-1}$) [8]. Thus, in RUN 1, the chosen gas mixture was Ne-CO_2 (90-10). The composition ratio was determined by the fact that at maximum drift field $400\,V\,cm^{-1}$ it maintains the maximum allowed drift time below $100\,\mu s$ and desired diffusion coefficients.

In RUN 2, instead of Ne-CO_2 (90-10), the chosen gas mixture was Ar-CO_2 (88-12), considering the fact that Ar provides higher operational stability than Ne. In this case, the other requirements mentioned above are also almost similar to the Neon-based gas composition.

Gas	Drift velocity v_d (cm/µs)	Diffusion coeff.		$\omega\tau$	Eff. ionization energy W_i (eV)	Number of electrons per MIP	
		D_L ($\sqrt{cm}$)	D_T ($\sqrt{cm}$)			N_p(primary) e/cm	N_t(total) e/cm
Ne-CO_2-N_2 (90-10-5)	2.58	0.0221	0.0209	0.32	37.3	14.0	36.1
Ne-CO_2 (90-10)	2.73	0.0231	0.0208	0.34	38.1	13.3	36.8
Ar-CO_2 (90-10)	3.31	0.0262	0.0221	0.43	28.8	26.4	74.8
Ar-CF_4 (90-10)	8.41	0.0131	0.0111	1.84	37.3	20.5	54.1

Table 1.2: Basic properties of gas mixtures applied in TPC. Diffusion coefficients are calculated at 400 V/cm. D_L and D_T represent the longitudinal diffusion coefficient and the transverse diffusion coefficient, respectively. $\omega\tau$ is the Lorentz angle. The table is taken from [8].

Furthermore, it is observed that adding a small dose (5 %) of N_2 to the Ne-CO_2 (90-10) composition brings a further improvement to the stability of the *readout chambers* at high gains. Therefore, the latest selection of gas mixture is Ne-CO_2-N_2 (90-10-5). Table 1.2 shows the basic properties of the various gas mixtures.

1.5   TPC upgrade

In RUN 3, the LHC will deliver Pb-Pb collisions with an interaction rate of 50 kHz. Different parts of the ALICE detector, such as readout electronics, have been upgraded to benefit from the increasing statistics. Although the TPC rate limitation was about 3.5 kHz in RUN 2, the readout rate was only a few hundred Hz due to limitations of the limited speed of the TPC electronics. Evidently, the gating mechanism of MWPC is unable to keep up with that high collision rate of RUN 3 [8].

Thus, the Gas Electrons Multiplier (GEM), a new amplification structure, has replaced the Multi-Wire Proportional Chamber to overcome this limitation. This GEM technology was first introduced by F. Sauli in 1996 [9].

A GEM foil is a composite grid of two thin metal (Copper) layers separated by a comparatively thicker insulating Polyimide film. In this case, the Polyimide film is 50 µm thick Kapton, and the Cu coating on each side has 5 µm thickness. A photo-lithographic process [11] perforates the foil to make a pattern of double conical holes(see Fig. 1.4). In brief,

(a) Top view of a GEM foil.
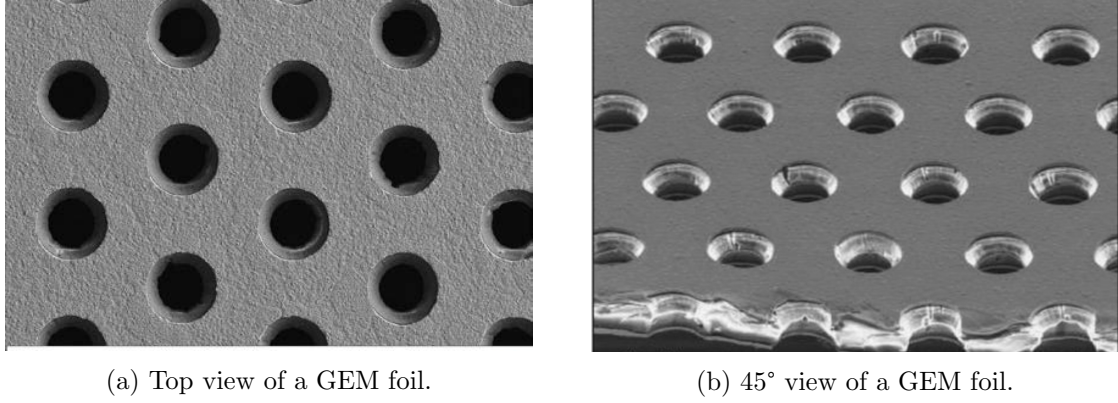
(b) 45° view of a GEM foil.

Figure 1.4: Microscopic view of a GEM foil [10].

photo-lithography is a process to transfer any geometric shape from a photomask to a photosensitive substance called photoresist. The inner (d) and outer diameter (D) of the double conical hole, in standard geometry, are 50 µm and 70 µm, respectively (See fig 1.5).
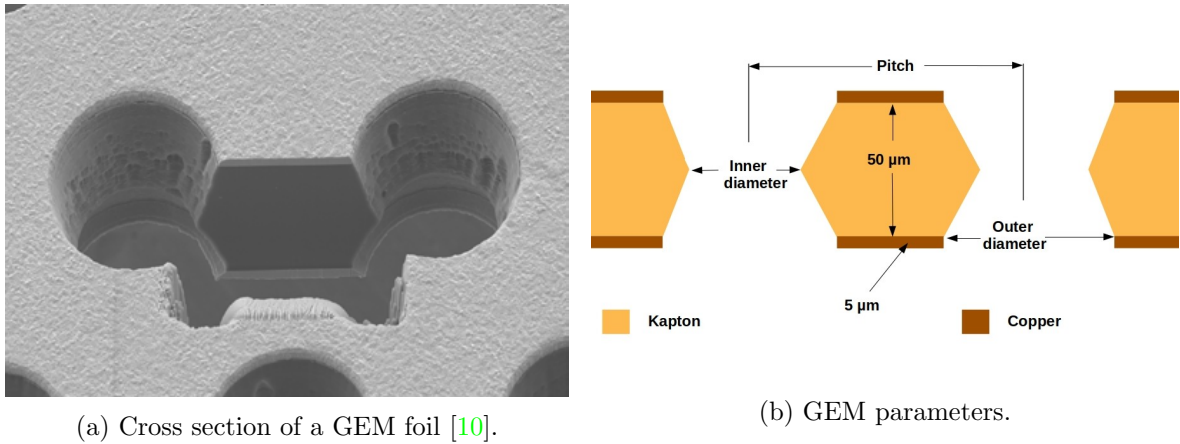

(a) Cross section of a GEM foil [10].

(b) GEM parameters.

Figure 1.5: Microscopic view of the cross-section of two neighboring GEM hole and the GEM parameters.

The Cu layers act as the top and bottom electrodes. The GEM holes can make an electron avalanche because of the presence of a high electric field. Electric field correlates with the GEM hole diameter. The narrower the hole, the stronger the field. As described before, GEM holes get narrower towards the middle. As a result, the strongest electric field is created in the middle of the hole. The high electric field can be produced by putting voltage difference between the top and the bottom electrode. As the field lines go from one electrode to another, the incoming electron gets accelerated through the hole and makes an avalanche. In the avalanche, a large number of electron-ion pairs are produced (see Fig. 1.7). The produced electrons travel towards the transfer field while the produced ions drift towards the drift volume.

The potential differences applied on the two electrodes of the GEMs (GEM voltage) and the transfer gap (Transfer field) between the neighboring GEMs as well as between GEM1 and cathode and between GEM4 and pad plane determine the movement of electrons and ions through the GEM system. They were configured in such a way so that an optimal output such as <1 % IBF, ≤12 % energy resolution ($\sigma(^{55}\text{Fe})$), 2000 gas gain, and operational stability can be achieved.
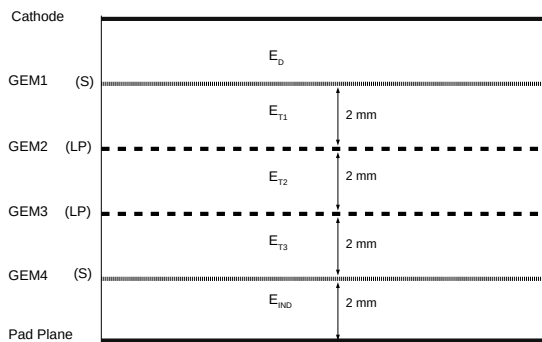
(a) The 4-GEM stack configuration.
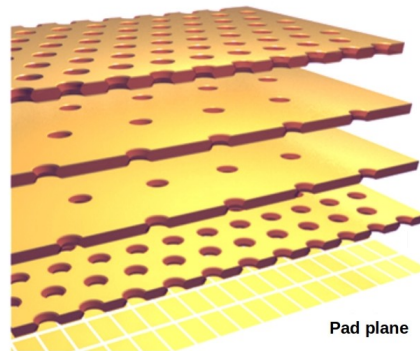
(b) A schematic view of the quadruple GEM stack [12].

Figure 1.6: In (a) E_D and E_{IND} stand for the drift field and field between GEM4 and pad plane, respectively. E_{Ti} corresponds to the transfer fields between the GEMs.

The upgrade design goal is to ensure non-gated continuous operation, keeping the number of back-drifting ions per extracted electron on the readout anode, the ion back-flow (IBF), $\leq 1\,\%$ at the same time. For this requirement, a stack of multiple GEMs, mounted on each other with $2\,\mathrm{mm}$ transfer field gap between them, is constructed (see Fig. 1.6). Hence, back drifting ions created in the lower GEMs get absorbed mainly by the bottom electrode of the upper GEMs. That is how the IBF can be minimized down to a tolerable level, resulting in better track reconstruction and distortion corrections. This intrinsic ion reduction mechanism, unlike MWPCs, produces no dead time.
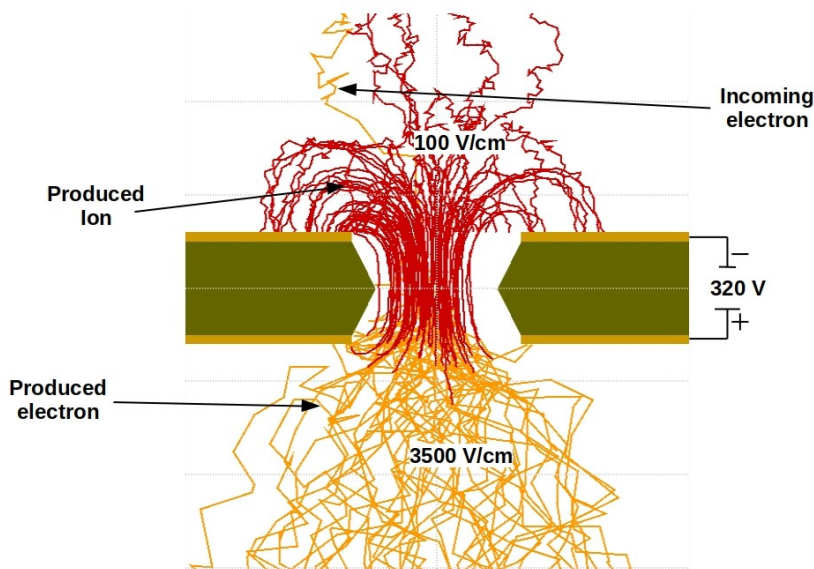

Figure 1.7: Example of Garfield simulation of an avalanche in a GEM hole by an incoming electron.

In this multiple GEM stack setting, IBF is calculated as the ratio between the number of ions that reach the drift region and the number of electrons that finally reach the pad plane. The number of ions that reach the drift region per incoming electron is called the ϵ value. The GEM foils also have some geometric variety. The distance between the center

of the two neighboring holes is called the pitch (see Fig. 1.5). GEMs with different pitch length were tested for the upgrade of the TPC. A combination of standard (140 μm) and large (280 μm) pitch GEMs was proposed as the baseline for the new TPC *readout chambers*. The configuration is S-LP-LP-S.

An important factor is the orientation of GEM holes between the neighboring GEM layers. IBF largely depends on it. If the holes of consecutive GEMs become aligned, the ion gets a favorable path through the GEMs to reach the drift region. As a result, a remarkable rise in IBF can be observed. However, if the holes are misaligned, a maximum number of ions end up on the bottom electrode of the next GEM, which reduces the IBF as expected. By keeping in mind that the GEM hole pattern follows a 60° rotational symmetry, this alignment issue can be countered by a 90° rotation of two consecutive GEM layers [13]. This issue only affects the ions because their movement is governed mainly by the electric field, not by diffusion. As far as the electron is concerned, their movement is guided mostly by diffusion. The correlation between alignment/misalignment and electron efficiencies fades away because of that.

Chapter 2

Simulation setup

The main goal of the thesis is to investigate electron and ion movement through a quadruple GEM stack. However, the simulation is done for each GEM separately, and later the results are combined to describe the properties of the full 4-GEM stack. A series for formulas is formed to combine these separately produced data from single GEM simulations. In this chapter the software used to simulate the electron and ion movements, the processes taken into account for the simulation, and other input information are described.

2.1 Software: Garfield++, Ansys etc

The main software for the simulation is Garfield++. It is an object-oriented tool for detailed simulation of particle detectors based on ionization measurement in gases or semiconductors [14, 15]. An interface to the Magboltz program [16, 17] is used to calculate the transport properties of the electrons. Different classes in Garfield++ for visualization purposes, such as plotting the drift lines, making contour plots of the potential, are also available, and they depend on the ROOT [18] framework. The simulation of electron avalanche is taken care of by semi-classical microscopic Monte Carlo simulation, which is based on the electron-atom/molecules cross-sections. In this method, an electron is followed from collision to collision. A table of collision rates for each scattering process as a function of electron energy is needed to accomplish this. A class called MediumMagboltz prepares and stores this information.
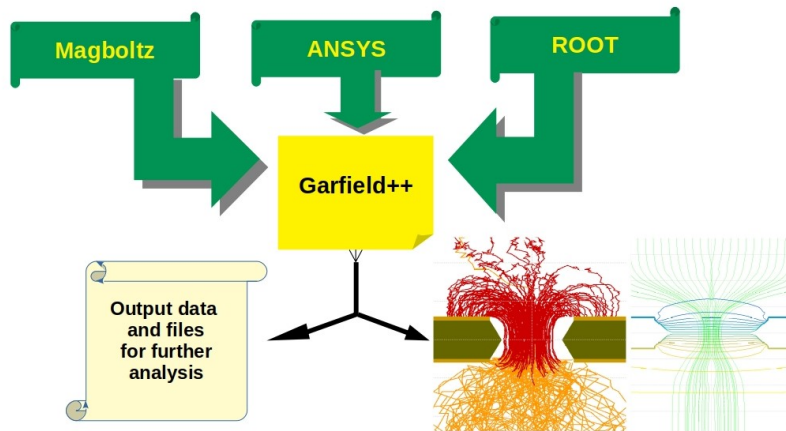

Figure 2.1: Flow of the simulation process.

The class AvalancheMicroscopic covers microscopic tracking of the electron. Ions, on

the other hand, cannot be tracked microscopically in Garfield++. Thus, the macroscopic transport properties (e.g., drift velocity, reduced electric field) of ions that are comparatively larger than those of the electron are provided by an ion-mobility file. The class that uses the information from the ion-mobility file and takes care of the ion track is called AvalancheMC. It also uses a Monte Carlo technique. A program called 'Heed' is available to simulate the ionization pattern along with the relativistic charged particles. The Photo-absorption ionization model has been implemented in this program, and the corresponding class is 'TrackHeed'. Another package named 'SRIM' is also available to simulate the ionization process created by low energy ions. ANSYS [19], an external field solver with a finite element method, is used for this project to calculate the electric field in the GEM. It divides the whole detector into a mesh of nodes and computes the electric field values at these nodes. ANSYS produces four text files named 'ELIST.lis', 'NLIST.lis', 'MPLIST.lis' and 'PNRSOL.lis'. 'ELIST.lis' contains the list of elements with pointers to the material property table and the node list. 'NLIST.lis' stores the node list with their position in the space. Moreover, the material property table that 'ELIST.lis' refers to is stored in the 'MPLIST.lis'. 'PNRSOL.lis' contains the estimated potential at each of the nodes. The classes that import those files and evaluate the electric field and potential for Garfield++ are ComponentAnsys121 or ComponentAnsys123. A simplified illustration of the flow of the simulation process is shown in Fig. 2.1.

2.2 Processes of electron and ion movement

Primary electrons move towards GEM1 and make an avalanche in the GEM hole. An example of the *avalanche* process can be seen in Fig. 2.2, where the drift paths of the electrons and ions are shown with the orange and red lines, respectively. In the avalanche, many electron-ion pairs are created. The ions created in the avalanche start going to the drift region. Some of them get absorbed by the top electrode of the GEM1. In the case of electrons, many of them get absorbed by the Kapton layer and the bottom electrode of GEM1 and some escape and reach GEM2. Some of these electrons get absorbed by the top electrode of GEM2. The rest of them move to the holes where they produce an avalanche again. The created electron-ion pairs in GEM2 follow the exact mechanism described before.
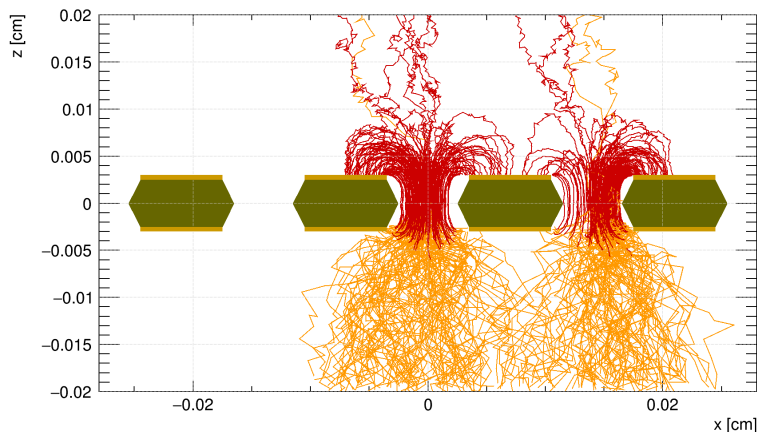

Figure 2.2: *Avalanche* process. The orange lines show the electron drift path and the red lines show the ion drift path.

In the case of ions that escaped from GEM2, some of them get captured by the top and bottom electrodes of GEM1, and a few of them join the other ions in the drift region. Extracted electrons from GEM2 make avalanche in GEM3 so does the extracted electron from GEM3 in GEM4. In all the cases, most of the ions get absorbed by the electrodes

whereas, some go through every GEM and reach the drift region. Thus, for each GEM, ions that reach the drift region have two contribution types, such as ions created in the avalanche in the same GEM foil and ions coming from other GEMs. The latter can be called the *ion transport* process. A visual representation of this process can be seen in Fig. 2.3 where the red lines show the ion drift path.

These two different processes are taken into account to calculate the total IBF for the 4-GEM stack. The ions created in the avalanche are named avalanche ions. However, the ions coming from the GEMs below can also contribute to the IBF. They are identified as the transported ion. The efficiencies of ions from these two processes are different because of their different origin points.
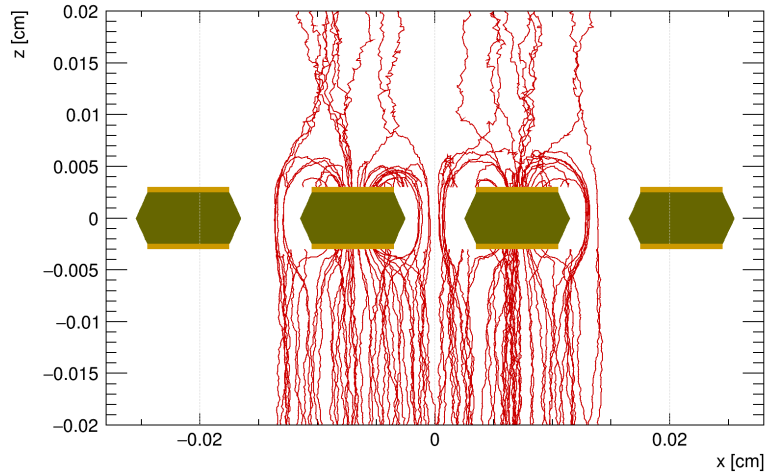
Figure 2.3: *Ion transport* process. The red lines show the ion drift path.

2.3 Voltage settings

In the simulation, the so-called voltage setting 'B' is used. It was defined during the commissioning of the TPC to increase operational stability. A simulation was also done in TDR addendum [13] to compare with the measurement of small-size prototype. The voltage setting used for that simulation (TDR setting) is also used in this thesis to repeat the TDR simulation and compare the data. Furthermore, the voltage setting used in a previous dedicated IBF measurement [20] (Measurement setting) in the Institut für Kernphysik Frankfurt [21], is used to carry out simulation for comparison and better understanding of the electron and ion transport parameters. These voltage settings are shown in Table 2.1. The electric field on the drift area E_D is $400\,\mathrm{V\,cm^{-1}}$ for each voltage settings.

	E_D (V/cm)	ΔU_{G1} (V)	ΔU_{G2} (V)	ΔU_{G3} (V)	ΔU_{G4} (V)	E_{T1} (V/cm)	E_{T2} (V/cm)	E_T (V/cm)	E_{IND} (V/cm)
B setting	400	270	230	320	320	3500	3500	100	3500
TDR setting	400	270	250	270	340	4000	2000	100	4000
Measurement setting	400	270	230	285	358	4000	4000	100	4000

Table 2.1: Voltage settings applied in the simulation. ΔU_{Gi} present the GEM voltages of their corresponding GEMs, and E_{Ti} are the transfer fields of the corresponding transfer gaps. E_{IND} is the field between GEM4 and the pad plane, and E_D is the drift field (see Fig. 1.6a).

13

An example of electric field lines going through GEM1 from the drift region to the induction gap is shown in Fig. 2.4.
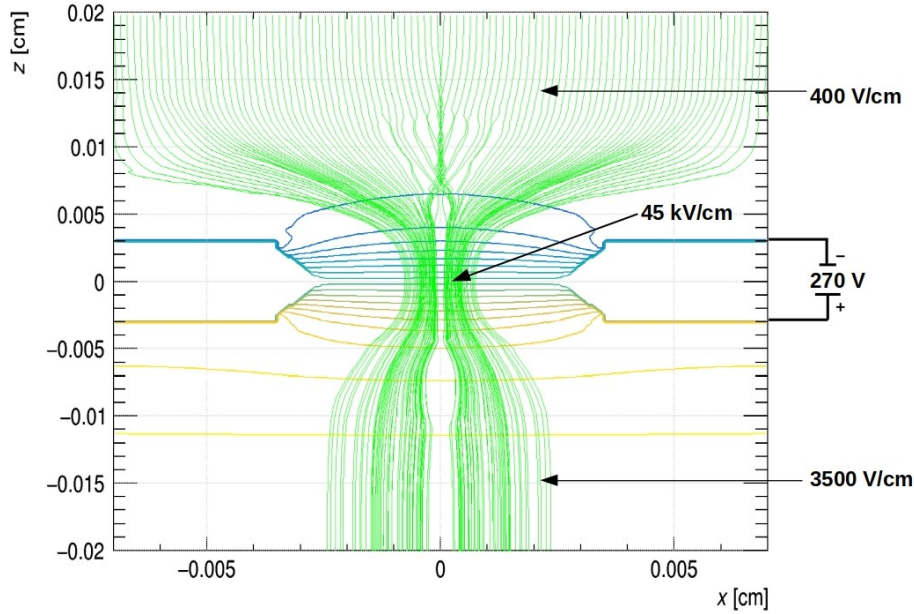

Figure 2.4: An example of electric field lines going through the GEM. The graphics created by Garfield++.

2.4   Gas mixture, Ion Mobility and Penning transfer probability

In the simulation, gas composition, temperature and pressure can be specified, and with the help of a class called 'MediumMagboltz', a gas file can be created. 'MediumMagboltz' is used to calculate transport parameters, and it is also the gateway to access the electron-molecule cross-sections, which help perform microscopic tracking. The chosen gas mixture for RUN3 is also used for this thesis simulation. The percentages of the components in the gas mixture are 85.72% Ne, 9.52% CO_2 and 4.76% N_2. The gas density is calculated in the form of temperature and pressure by using ideal gas law. Magboltz interface calculates the transport properties by using semi-classical Monte Carlo simulation. The gas file contains the transport properties of the gas for electrons and a table that stores the collision frequencies of excitation and ionization levels.

Unlike electrons, ions cannot be tracked microscopically in Garfield++. Therefore, the ion-mobility data must be entered by hand. An ion-mobility file is used in the simulation to solve this issue. In this 'txt' file, a table of reduced electric fields and their corresponding reduced ion mobility of Ne^+ in pure Ne are stored (see Fig. 2.5). The ion mobility (K) is defined as the result of drift velocity divided by the drift field:

$$K = \frac{V_{drift}}{E_{drift}} \tag{2.1}$$

Another adjustable parameter important for the simulation is the penning transfer probability. When a free electron collides with a neutral noble gas atom (X), the following
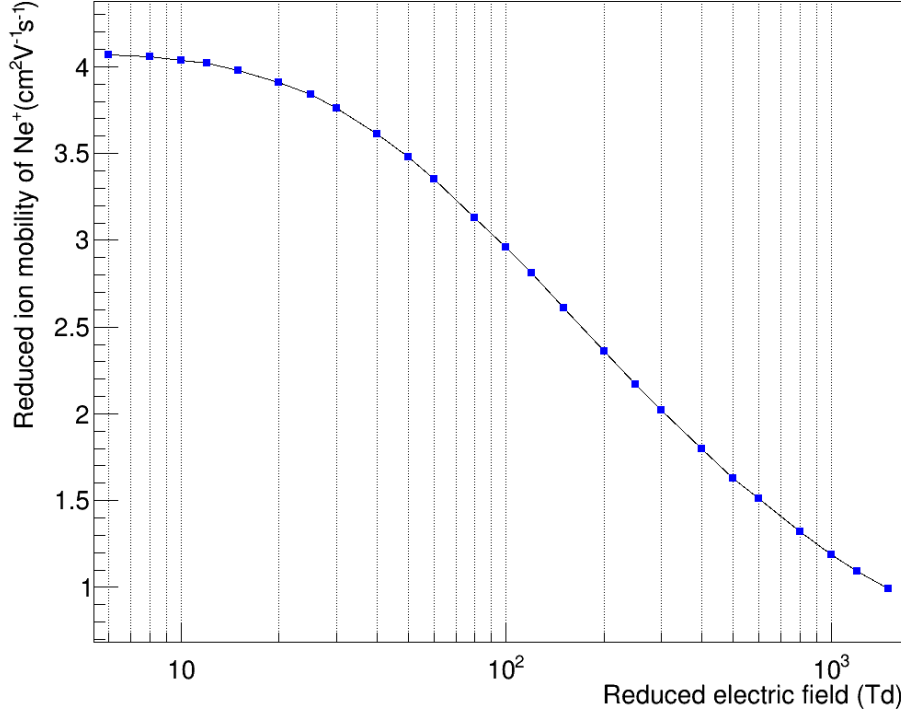
Figure 2.5: Reduced mobility of Ne^+ in pure Ne as a function of reduced electric field [7].

mechanisms may happen:

$$e^- + X \rightarrow e^- + e^- + X^+ \tag{2.2}$$

$$e^- + X \rightarrow e^- + X^* \tag{2.3}$$

The excited energy state of the noble gas (X^*) can contribute to the avalanche by transferring their energy to an admixture gas (Y). This process is called penning transfer [22]. X^+ and Y^+ are the ions of their corresponding gases.

$$X^* + Y \rightarrow X + Y^+ + e^- \tag{2.4}$$

In a gas mixture, penning transfer happens if the metastable excitation energy level of a component is energetically higher than the other component's ionization energy. Neon has

	Ne	CO_2
Excitation levels	16.7 eV 18.65 eV 19.75 eV 20.1 eV	
Ionnization energy	21.56 eV	13.78 eV

Table 2.2: Excitation and ionization potentials of Ne and CO_2 [23].

multiple excitation levels, and their energy levels are higher than the ionization potential of CO_2 (see Table 2.2). It makes the penning transfer possible and brings more operational stability. The number of produced electron-ion pairs increases with the increase of penning transfer probability. As a result, factors related to gas amplification, such as gain, also increase.

As our simulation deals with each GEM foil separately, there is no need to achieve misalignment by rotating the GEM. However, the effect of this modification cannot be ignored. This problem is solved by randomizing the initial positions of the input electrons and, in the case of *ion iransport* process, the initial position of input ions. Because of the randomization, the probability of alignment effect mostly vanishes, and the ion movement scenario gets closer to the actual situation.

Chapter 3

Results, Analysis and comparison

In this chapter, the necessary transport parameters are defined and the formulas to describe the transport properties are formed. After that, the procedure of extracting transport parameter data from the simulation is described. Later, an analysis of the transport parameters for different voltage settings is given.

3.1 Transport properties of a 4-GEM stack

In the simulation, some primary electrons can be put in the upper end of the drift region from where they travel towards the GEM into the GEM hole to make amplification. From the amplification region, the newly created secondary electrons and ions move in opposite directions. The two processes (*avalanche* and *ion transport* processes) described in Section 2.2, are taken into account to define the parameters and to prepare the formulas.
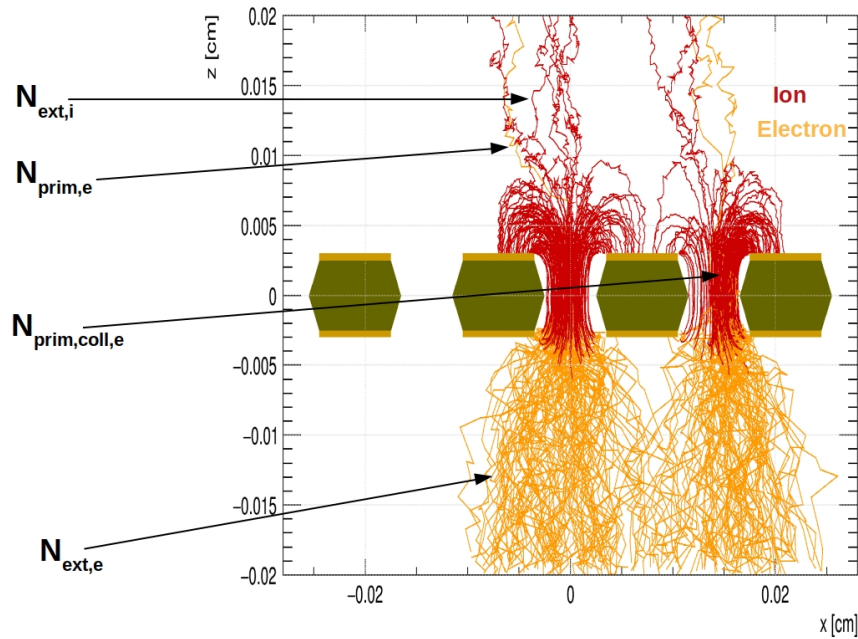
Figure 3.1: Classification of electrons and ions in the *avalanche* process according to their end points.

Some of the incoming primary electrons end up directly on the upper electrode of the GEM, while the rest of them successfully go into the GEM holes. The latter part of the

primary electrons is called the collected electrons ($N_{prim,coll,e}$). The ratio between the number of collected electrons and the number of total primary electrons ($N_{prim,e}$) is called the collection efficiency of electrons ($\varepsilon_{coll,e}$):

$$\varepsilon_{coll,e} = \frac{N_{prim,coll,e}}{N_{prim,e}} \tag{3.1}$$

Secondary electrons produced in the avalanche can either get captured by the Kapton wall and the bottom electrode or escape the GEM. Escaped electrons move towards the next GEM. A small portion of them gets attached by the gas molecule on the way while the rest of them reach the next GEM or, in the case of GEM4, the pad plane. Those electrons that reach the next GEM are called extracted electrons. The ratio between the number of extracted electrons ($N_{ext,e}$) and the total produced electrons ($N_{produced,e}$) is defined as the extraction efficiency of electrons ($\varepsilon_{ext,e}$):

$$\varepsilon_{ext,e} = \frac{N_{ext,e}}{N_{produced,e}} \tag{3.2}$$

Another important parameter called Multiplication (M) is defined as the ratio between the number of total produced electrons and the number of collected electrons:

$$M = \frac{N_{produced,e}}{N_{prim,coll,e}} \tag{3.3}$$

Finally, the effective gain (G_{eff}) is defined as the product of collection efficiency of electron, multiplication, and extraction efficiency of the electrons:

$$G_{eff} = \varepsilon_{coll,e} \times M \times \varepsilon_{ext,e} = \frac{N_{ext,e}}{N_{prim,e}} \tag{3.4}$$

Now, in the case of ions produced in the avalanche, some can be absorbed by the GEM, whereas the rest of them are extracted to the transfer gap or the drift area. The latter mentioned type of ions is called extracted ions ($N_{ext,i}$). The extraction efficiency of ions ($\varepsilon_{ext,i}$), as for the electrons, is defined as a ratio between the number of extracted ions and the total number of produced ions ($N_{produced,i}$):

$$\varepsilon_{ext,i} = \frac{N_{ext,i}}{N_{produced,i}} \tag{3.5}$$

A graphical representation of all the above mentioned electron and ion types can be see in Fig. 3.1.

In the case of ions from the *ion transport* process, input ions ($N_{in,i}$) start going towards the GEM from the lower end of the transfer gap under the guidance of the electric field. Some of them get absorbed by the bottom electrode of the GEM ($N_{b,i}$). The rest of the ions, on the other hand, go through the GEM hole and either get absorbed by the top electrode ($N_{t,i}$) or continue moving towards the next GEM ($N_{ext,i}$). The summation of the number of ions ended up on top electrode ($N_{t,i}$) and the number of extracted ions ($N_{ext,i}$) is called collected ions ($N_{coll,i}$) (see Fig. 3.2). Therefore, the collection efficiency of ions ($\varepsilon_{coll,i}$) is defined as the ratio between the number of collected ions and the number of total input ions.

$$N_{coll,i} = N_{t,i} + N_{ext,i} \tag{3.6}$$

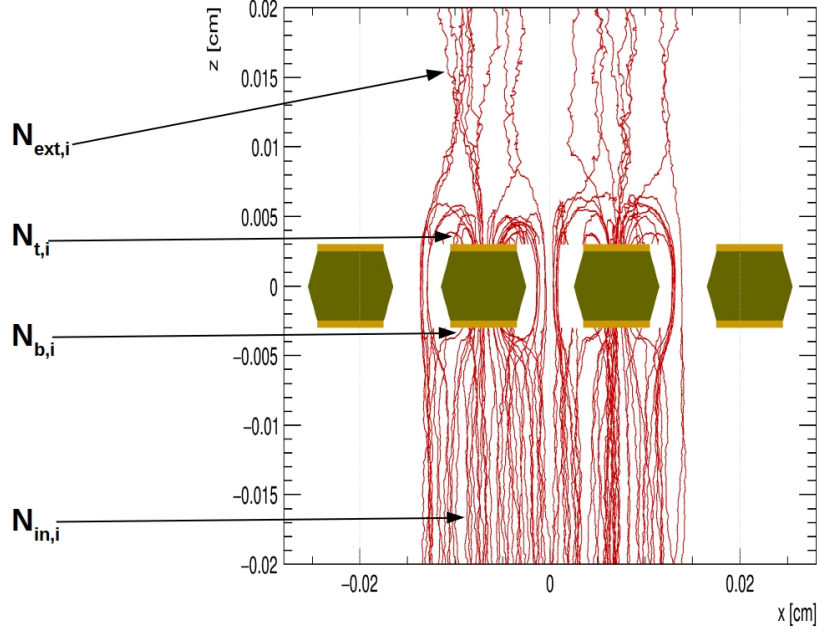$$\varepsilon_{coll,i} = \frac{N_{coll,i}}{N_{in,i}} \tag{3.7}$$

Figure 3.2: Classification of ions in the *ion transport* process based on their end points.

The extraction efficiency of the ions ($\varepsilon_{ext,i}$) is defined as the ratio between the number of extracted ions and the number of collected ions.

$$\varepsilon_{ext,i} = \frac{N_{ext,i}}{N_{coll,i}} \tag{3.8}$$

Another parameter called the transfer efficiency of ions ($\varepsilon_{tr,i}$) results from dividing the number of extracted ions by the number of total input ions. $\varepsilon_{tr,i}$ represents the ions that come from another GEM, move through the GEM hole and finally escape to the transfer gap.

$$\varepsilon_{tr,i} = \frac{N_{ext,i}}{N_{in,i}} = \frac{N_{coll,i}}{N_{in,i}} \times \frac{N_{ext,i}}{N_{coll,i}} = \varepsilon_{coll,i} \times \varepsilon_{ext,i} \tag{3.9}$$

The number of extracted electrons for each GEM can be written as follow:

$$N_{ej} = N_{prim,e} \times \varepsilon_{coll,ej} \times M_{Gj} \times \varepsilon_{ext,ej} = N_{prim,e} \times G_j \tag{3.10}$$

Here, j represents the GEM number (1 to 4) and N_{ej} describe the number of extracted electrons from their corresponding GEMs.

Another series of formulas is established to estimate the final contribution of the ions in the 4-GEM stack. On the right-hand side of the equation (3.11), (3.12), (3.13) and (3.14), the black part represents the contribution of electron created in the avalanche. The blue and red parts correspond to the contribution of ions produced in the avalanche and ions coming from another GEM, respectively. N_{i1}, N_{i2}, N_{i3} and N_{i4} represent the contribution of ions to the drift region from GEM1, GEM2, GEM3 and GEM4 respectively. A simple illustration of the complete process in a 4-GEM stack is drawn in Fig. 3.3.

$$
\begin{aligned}
N_{i1} &= N_{prim,e} \times \varepsilon_{coll,e1} \times M_{G1} \times \varepsilon_{ext,i1} & (3.11)\\
N_{i2} &= N_{e1} \times \varepsilon_{coll,e2} \times M_{G2} \times \varepsilon_{ext,i2} \times \varepsilon_{tr,i1} & (3.12)\\
N_{i3} &= N_{e2} \times \varepsilon_{coll,e3} \times M_{G3} \times \varepsilon_{ext,i3} \times \varepsilon_{tr,i2} \times \varepsilon_{tr,i1} & (3.13)\\
N_{i4} &= N_{e3} \times \varepsilon_{coll,e4} \times M_{G4} \times \varepsilon_{ext,i4} \times \varepsilon_{tr,i3} \times \varepsilon_{tr,i2} \times \varepsilon_{tr,i1} & (3.14)
\end{aligned}
$$

19
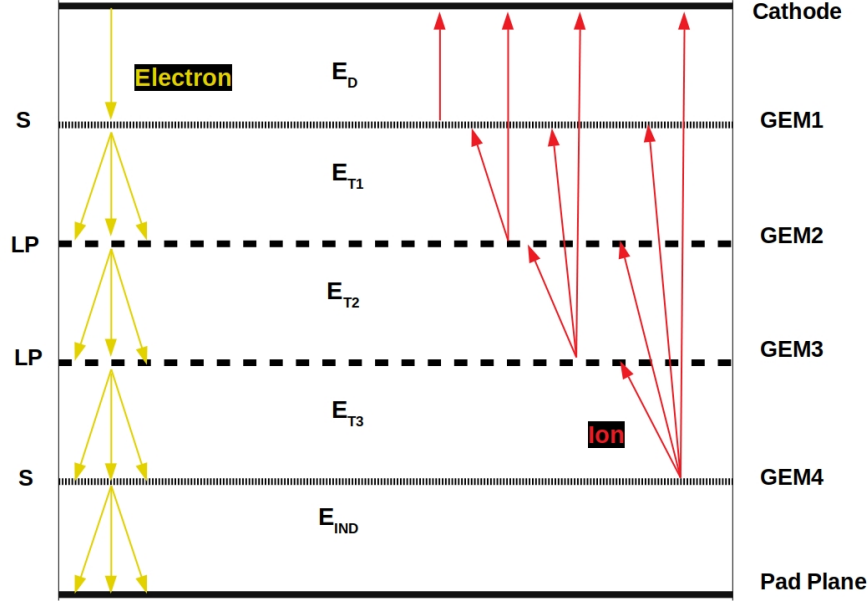
Figure 3.3: A simple illustration of electron and ion flow through the quadruple GEM stack. E_D, E_{Ti}, and E_{IND} stand for the applied transfer fields of drift zone, between the consecutive GEMs and between GEM4 and the pad plane respectively.

The IBF of a 4 GEM stack is defined as [8]:

$$IBF = \frac{1 + \epsilon}{G_T} \tag{3.15}$$

Here, the total effective Gain (G_T) is calculated by multiplying the gain of all four GEMs.

$$G_T = G_1 \times G_2 \times G_3 \times G_4 \tag{3.16}$$

The ion space-charge density parameter ϵ being the number of ions entering the drift zone per incoming electron, is defined as follows:

$$\epsilon = \frac{N_{i1} + N_{i2} + N_{i3} + N_{i4}}{N_{prim,e}} \tag{3.17}$$

3.2   Data extraction from the simulation

In this section, the process of extracting the data from the simulation that are used to calculate the transport parameters is described. After that, these parameters are used in the formulas that calculate the IBF for a 4-GEM stack.

Electrons are tracked from collision to collision with the help of implemented tracking method in the class 'AvalancheMicroscopic'. The numbers of produced electrons and ions are given by the 'GetAvalancheSize' in the simulation. 'GetElectronEndpoint' returns the coordinates and time of the start and end points of electron drift lines. A list of so-called 'status' codes is available in Garfield++ to indicate why the tracking of an electron or ion is stopped. It is used in 'GetElectronEndpoint' class. The endpoints of electrons can be located from this class. Another class called 'GetIonEndpoint' has the similar parameters that can be used to get the endpoints of the ions. The list of status code is given in Table 3.1.

status code	meaning
−1	particle left the drift area
−3	calculation abandoned (error, should not happen)
−5	particle not inside a drift medium
−7	attachment
−8	sharp kink (only for RKF)
−16	energy below transport cut
−17	outside the time window

Table 3.1: Status codes for the termination of drift lines. This table is obtained from the Garfield++ user guide [14].

For example, status −5 and −7 indicate the secondary electrons absorbed by the Kapton or copper and the electrons absorbed by the gas molecule while traveling towards the next GEM, respectively. A code of −1 refers to the electrons that finally reached the next GEM. The rest of the status codes are not relevant for the analysis.

All the data needed to calculate the transport parameters can be obtained by analyzing the endpoints and the status code. For example, with voltage setting 'B', the fractions of the

	Electrons absorbed by the GEM (-5) (%)	Attachment (-7) (%)	Electrons reach the next GEM (-1)(%)	Attachment rate (electron/cm)
GEM 1	49.3	2.8	47.8	0.27
GEM 2	66.4	2.2	31.4	0.21
GEM 3	88.8	0.37	10.8	0.04
GEM 4	48.8	2.9	48.3	0.28

Table 3.2: Estimation of the endpoints of the electrons according to different status code. The data collected from the simulations that are done with voltage setting 'B'.

totally produced electrons that get absorbed by the GEM, attached, or reach the next GEM are shown in Table 3.2. Electrons get attached while moving through the transfer gap. It is observed that the distribution of the attached electron is uniform throughout the whole path (see Fig. 3.4b). Thus, the rate of attachment per unit length (cm) for each GEM is also given in Table 3.2. In the simulation, the GEM is put on an XY plane. Thus, the Z-axis is perpendicular to the GEM. The GEM covers the length from $30\,\mu m$ (top of the top electrode) to $-30\,\mu m$ (bottom of the bottom electrode) along the Z coordinate. The drift gap and the induction gap both are $1\,mm$. A cut is put from $30\,\mu m$ to $-30\,\mu m$ to get the number of primary electrons that enter the GEM hole. With the help of status code −1 and a proper cut along the Z direction, the number of extracted electrons is calculated. For example, the endpoints of the electrons created in a standard pitch GEM with voltage setting 'B' (GEM1) can be seen in Fig. 3.4.

In the case of ion produced in the amplification, status codes are also applicable. The GEM absorbs some of the produced ions and the rest of them reaches the drift volume. There is no ion absorbed by attachment. For example, in Fig. 3.5, the endpoints of ions produced in the avalanche in a standard pitch GEM with voltage setting 'B' (GEM1) can be seen. Figure 3.5b shows that there is no ion corresponds to status code −7. The number of extracted ions is calculated by using the status code -1.
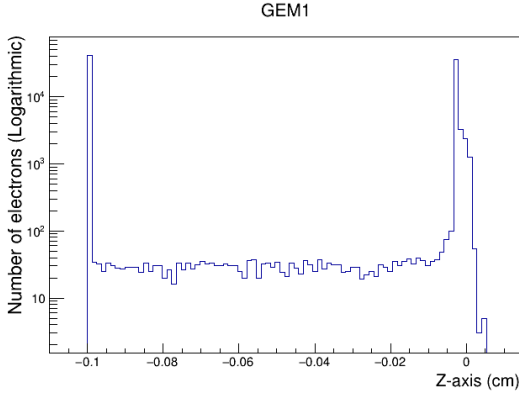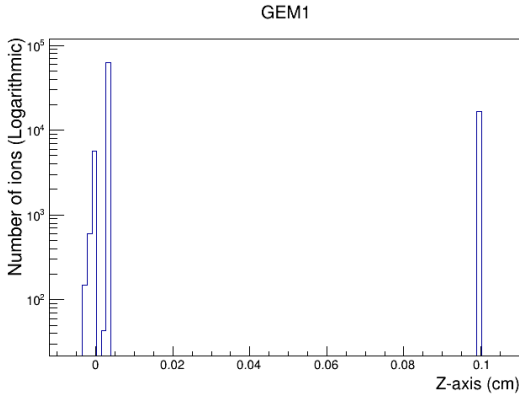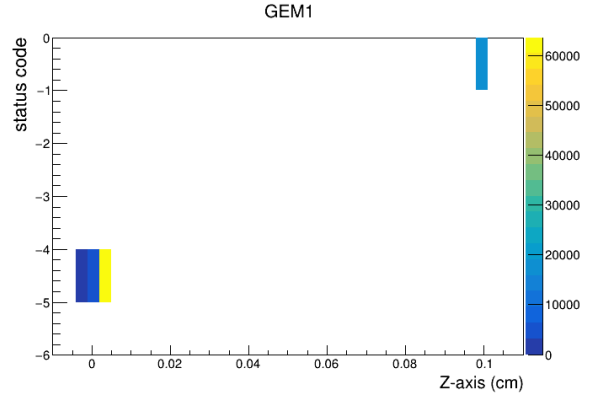
(a) Electron endpoints
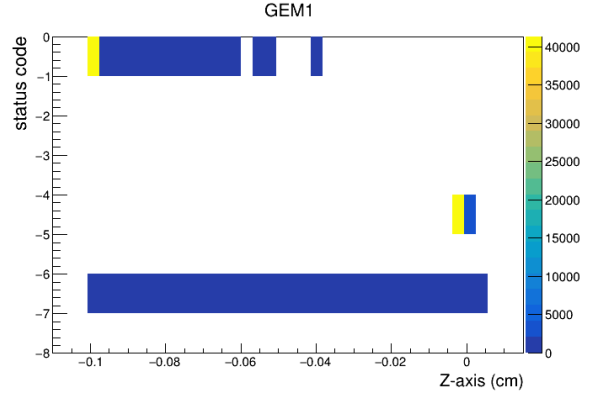
(b) Electron endpoints according to their corresponding status code.

Figure 3.4: End points of the electrons created in the *avalanche* process in GEM1. The colored bar in figure (b) shows the number of electrons. GEM with standard pitch length, 270 V ΔU_G, 400 V cm^{-1} E_D and 3500 V cm^{-1} E_{IND} is used.

(a) Ion endpoints.

(b) Ion endpoints according to their corresponding status code.

Figure 3.5: End points of the ions created in the *avalanche* process. The colored bar in figure (b) shows the number of ions. GEM with standard pitch length, 270 V ΔU_G, 400 V cm^{-1} E_D and 3500 V cm^{-1} E_{IND} is used.

In the *ion transport* process, the number of transferred ions is calculated from the simulation. In Fig. 3.6, an example of the endpoints of ions moving through a standard pith GEM with voltage setting 'B' (GEM1) can be seen. As well as the other process, status code -1 represents the ions that drift through the GEM and go to the next GEM or to the drift volume (in the case of GEM1).

(a) Ion endpoints.

(b) Ion endpoints according to their corresponding status code.
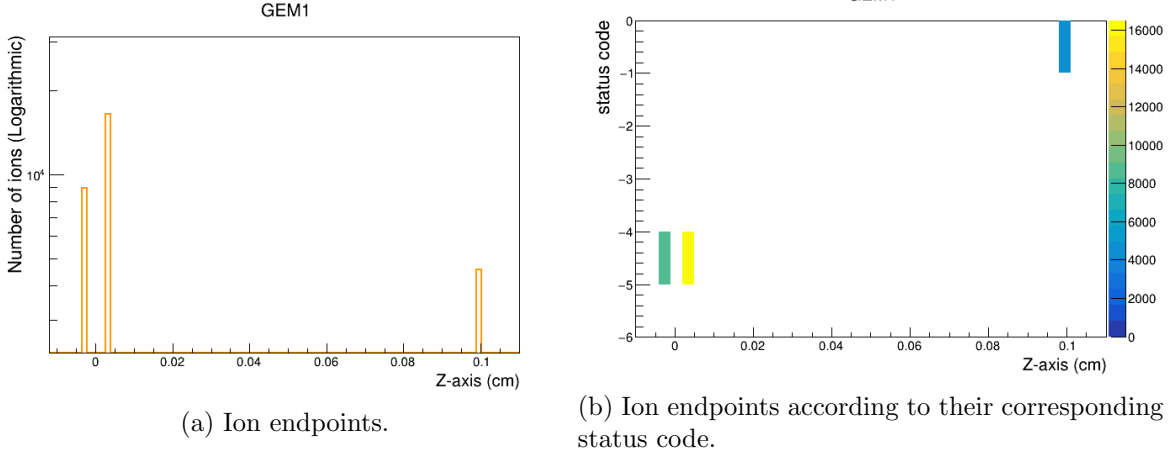
Figure 3.6: Endpoints of the ions coming from another GEM (*ion transport* process). The colored bar on the right side shows the number of ions. GEM with standard pitch length, 270 V ΔU_G, 400 V cm^{-1} E_D and 3500 V cm^{-1} E_{IND} is used.

3.3 Data analysis with Voltage setting 'B'

In this section, various transport parameters and their trends for each GEM foil are presented. They are calculated with the data extracted from the simulation (see Section 3.2). The simulation is done with voltage setting 'B' and 85 % penning transfer probability. For each GEM, $N_{prim,e}$ is 3000 in the *avalanche* process and $N_{in,i}$ is 30 000 in the *ion transport* process. (See Fig. 1.6a) The transport parameters greatly depend on the GEM voltage (ΔU_G), the

	E_D (V/cm)	ΔU_{G1} (V)	ΔU_{G2} (V)	ΔU_{G3} (V)	ΔU_{G4} (V)	E_{T1} (V/cm)	E_{T2} (V/cm)	E_T (V/cm)	E_{IND} (V/cm)
B setting	400	270	230	320	320	3500	3500	100	3500

Table 3.3: Voltage settings applied in the simulation. ΔU_{Gi} present the GEM voltages of their corresponding GEMs, and E_{Ti} are the transfer fields of the corresponding transfer gaps. E_{IND} is the field between GEM4 and the pad plane, and E_D is the drift field.

field above the GEM (E_{TA}) and the field below the GEM (E_{TB}). For example, the collection efficiency of primary electrons ($\varepsilon_{coll,e}$) greatly depends on E_{TA}. As can be seen in Fig. 3.7a, the $\varepsilon_{coll,e}$ tends to be almost 100 % for GEM1 and GEM4 that have low E_{TA} whereas, it is below 20 % for GEM2 and GEM3 that have high E_{TA}. It is clear that with a higher E_{TA}, the $\varepsilon_{coll,e}$ gets lower and vice versa. It can be assumed that in the case of higher E_{TA}, the incoming electrons are not highly focused on the GEM holes. Thus, they get absorbed by the top electrode. Moreover, GEM1 and GEM4 have the standard pitch (140 µm), unlike GEM2 and GEM3 that have a large pitch (280 µm). Therefore, GEM1 and GEM4 have higher hole densities than GEM2 and GEM3. As a result, the incoming electron's probability to enter the holes to make an avalanche is higher.

Figure 3.7b shows the opposite trend than that of $\varepsilon_{coll,e}$. It shows the extraction efficiency of ions $\varepsilon_{ext,i}$ that are created in the *avalanche* process (see Section 2.2). The trend shows that $\varepsilon_{ext,i}$ increases with the increasing E_{TA}. A slight decrease of the $\varepsilon_{ext,i}$ from GEM2 to GEM3 can be seen. Although they have the same E_{TA} (3500 V cm^{-1}) above them, their ΔU_G are significantly different (ΔU_{G2}=230 V and ΔU_{G3}=320 V). As explained in Section 2.3 higher GEM voltage corresponds to larger amplification. However, in GEM3, it is also observed in the simulation that the absorption rate of ions by the Kapton wall and the top electrode is almost twice as much as the rate in GEM2. Consequently, a slightly lower $\varepsilon_{ext,i}$ is observed
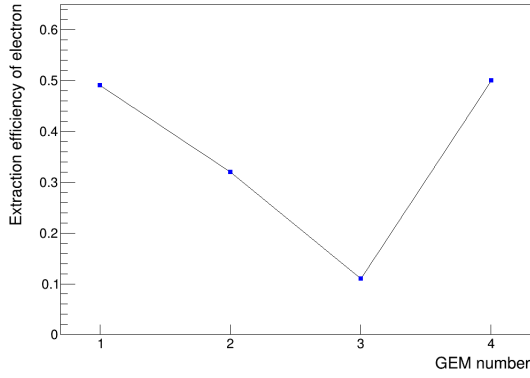
23
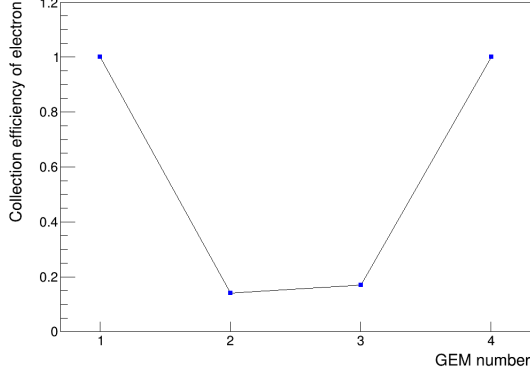
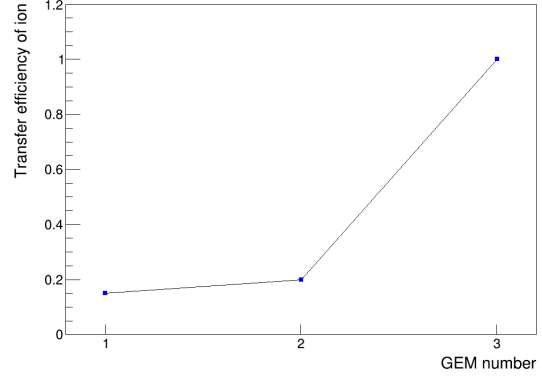(a) Collection efficiency of electrons.
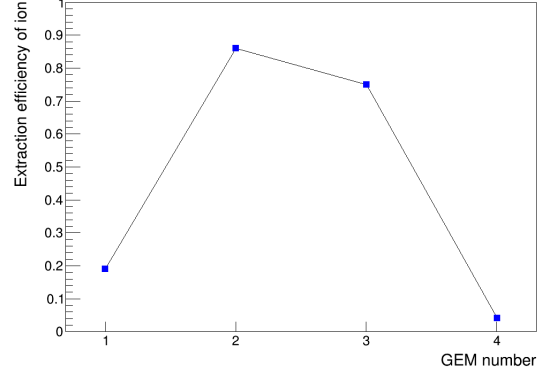
(b) Extraction efficiency of ions.

Figure 3.7: Changing pattern of $\varepsilon_{coll,e}$ and $\varepsilon_{ext,i}$ from GEM1 to GEM4.

for GEM3. Although GEM4 has the same ΔU_G as GEM3, its $\varepsilon_{ext,i}$ is lower than any other GEM because of extremely low E_{T3}.

(a) Extraction efficiency of electrons.

(b) Transfer efficiency of ions.

Figure 3.8: Changing pattern of $\varepsilon_{ext,e}$ and $\varepsilon_{tr,i}$ (*ion transport* process) from GEM1 to GEM4.

Figure 3.8a depicts the extraction efficiency of the electrons ($\varepsilon_{ext,e}$). $\varepsilon_{ext,e}$ depends on the applied E_{TB} and the ΔU_G. $\varepsilon_{ext,e}$ decreases with the decrease of E_{TB} and vice-versa. As E_{T2} is 35 times higher than E_{T3}, GEM3 has lower $\varepsilon_{ext,e}$ than GEM2. It can be said that the influence of E_{TB} is more dominant than the influence of ΔU_G on $\varepsilon_{ext,e}$. Low E_{TB} forces electrons to end up on bottom electrode of the GEM. That can be an explanation for GEM4 having much higher $\varepsilon_{ext,e}$ than GEM3, although they have the same GEM voltages (320 V). GEM2's $\varepsilon_{ext,e}$ is much lower than GEM1. ΔU_{G2} is much lower than the ΔU_{G3} although, they have the same E_{TB}. A possible explanation can be that a lower field inside the GEM hole leads to a larger diffusion. As a result, a large part of the produced electron can reach the GEM wall and get absorbed resulting in a low $\varepsilon_{ext,e}$. Moreover, GEM1 and 2's different pitch length can also effect $\varepsilon_{ext,e}$.

In Fig. 3.8b, the change of transfer efficiency $\varepsilon_{tr,i}$ is shown. It is related to the *ion transport* process (see Section 2.2). It is also influenced by E_{TB} as the ions come from below the GEM. $\varepsilon_{tr,i}$ increases with the decrease of E_{TB}. The reason can also be that the ions are not highly focused on the GEM holes under the high transfer field.

As discussed before, production of electron-ion pairs largely depends on the GEM voltage,

(a) Effective gain
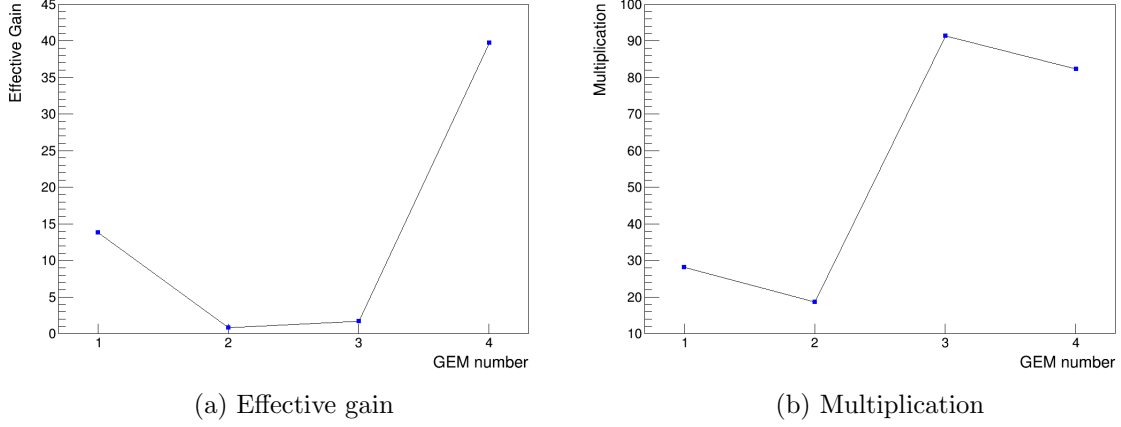
(b) Multiplication

Figure 3.9: Changing pattern of Effective gain and Multiplication from GEM1 to GEM4.

and the extraction efficiency of electrons highly depends on the E_{TB}. In equation (3.4), it can be seen that effective gain is the product of $\varepsilon_{coll,e}$, M and $\varepsilon_{ext,e}$. All these parameters go down from GEM1 to GEM2. Therefore, the effective gain goes down from GEM1 to GEM2. For GEM3, the effective gain slightly increases although its $\varepsilon_{ext,e}$ is much lower than that of GEM2. It is because GEM3's M is almost 5 times higher than GEM2's. From GEM3 to GEM4, the effective gain goes up although they have the same ΔU_G (see Fig. 3.9a). It is because the E_{IND} is considerably higher than E_{T3} leading to a higher extraction efficiency. In addition, GEM3 and GEM4's different GEM type might also have some effect on this.

In Fig. 3.9b, the variation of Multiplication from GEM1 to GEM4 is presented. It rises

(a) IBF
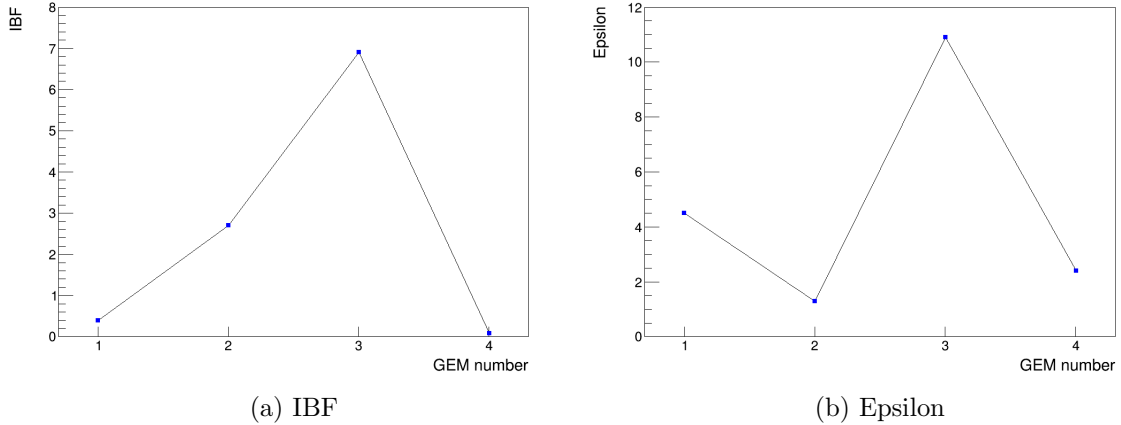
(b) Epsilon

Figure 3.10: Changing pattern of IBF and Epsilon value from GEM1 to GEM4.

with the rise of ΔU_G as expected. Although GEM3 and GEM4 have the same ΔU_G, the multiplication is lower in GEM4. It might be because of their different pitch lengths and different E_{TA} and E_{TB}s. However, it was not investigated in detail.

The IBF for single GEM foils shown in Fig. 3.10a. The trend can be easily understood by looking at the change of $\varepsilon_{ext,i}$ and $\varepsilon_{ext,e}$ with high and low E_T. Finally, in Fig. 3.10b, the changing pattern of the number of extracted ions per incoming electron (ϵ) is presented. For the 4 GEM stack, the total effective gain is 786.5, ϵ is 16 and the IBF is 2.2 %.

3.4 A scan through the penning transfer probability

Penning transfer probability is a parameter described in Section 2.4. It can be tuned from 0 to 100 % for optimization of the simulation data. Therefore, a coarse scan for the Effective gain, Multiplication, IBF, and epsilon for each GEM is performed through the complete penning transfer range to investigate the influence of penning transfer on the parameters and further data optimization. The results are shown in Fig. 3.11 and 3.12.
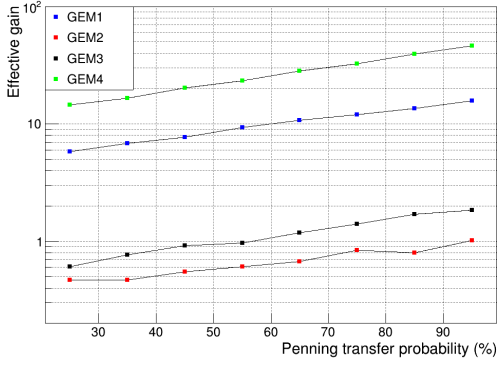
(a) Effective gain of single GEM foils as a function of penning transfer probability.
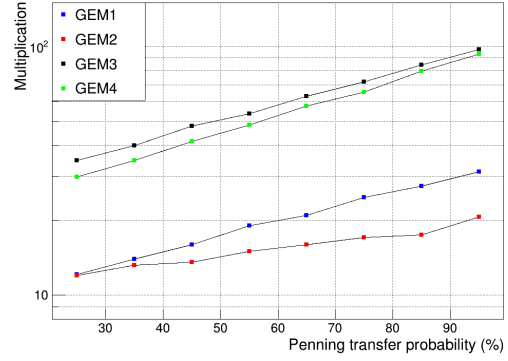
(b) Multiplication of single GEM foils as a function of penning transfer probability.

Figure 3.11: Changing pattern of effective gain, multiplication for single GEM foils with the increasing penning transfer probability.
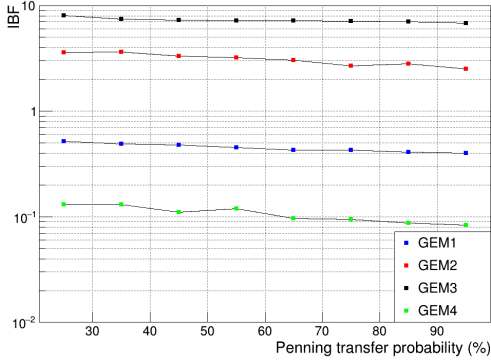
(a) IBF of single GEM foils as a function of penning transfer probability
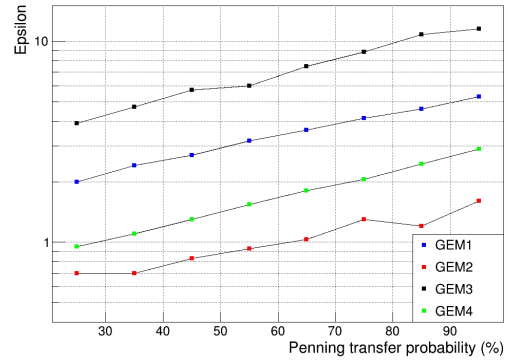
(b) Epsilon value of single GEM foils as a function of penning transfer probability

Figure 3.12: Changing pattern of IBF and epsilon value for single GEM foils with the increasing penning transfer probability.

Effective gain increases with the increase of penning transfer probability for each GEM foil (Fig. 3.11a) while the IBF goes down (Fig. 3.12a). The multiplication also rises as higher penning transfer probability contributes to producing a higher number of electron-ion pairs. This correlation between penning transfer probability and amplification also explains the higher number of extracted ions per incoming electrons with the increasing penning transfer probability. The $\varepsilon_{coll,e}$ and $\varepsilon_{ext,e}$ for each GEM remain unchanged throughout the whole penning transfer probability range.

Although the effective gain increases with the increase of penning transfer which increases total effective gain for 4-GEM stack, it does not reach 2000 (see Fig. 3.13a). The IBF (see

Fig. 3.13b) and the epsilon value (see Fig. 3.13c) for the 4-GEM stack also follow the same trend as their single GEM counterparts. The total effective gain is 1363 at 95 % penning transfer probability. The corresponding IBF is 1.7 % and the epsilon is 22. The
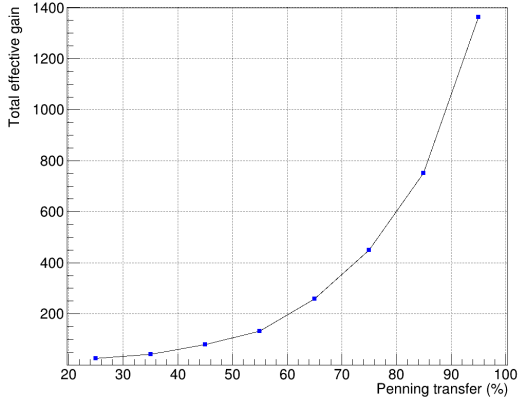
(a) Total effective gain of the 4-GEM stack as a function of penning transfer probability.
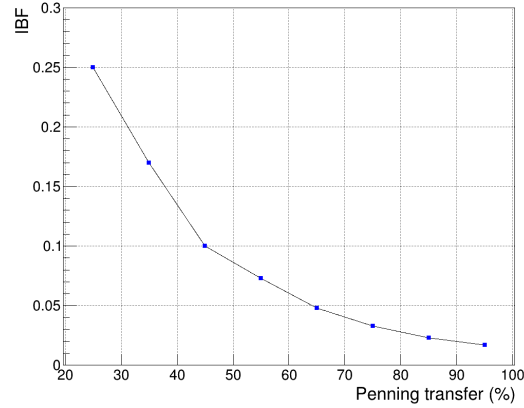
(b) IBF of the 4-GEM stack as a function of penning transfer probability.
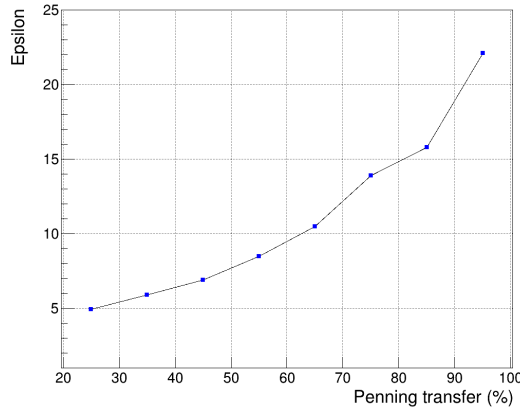
(c) Epsilon value of the 4-GEM stack as a function of penning transfer probability.

Figure 3.13: Changing pattern of total effective gain, IBF and epsilon of 4-GEM stack with the increasing penning transfer probability.

3.5 Comparison with the TDR simulation

In the TDR addendum [13], a dedicated comparison of simulations and measurements with small-size prototypes was done. The voltage setting applied in TDR simulation is shown in Table 3.4. The results of that comparison is shown in Table 3.5.

	E_D (V/cm)	ΔU_{G1} (V)	ΔU_{G2} (V)	ΔU_{G3} (V)	ΔU_{G4} (V)	E_{T1} (V/cm)	E_{T2} (V/cm)	E_{T3} (V/cm)	E_{IND} (V/cm)
TDR setting	400	270	250	270	340	4000	2000	100	4000

Table 3.4: Voltage settings applied in the TDR simulation.

	ε_{coll}	$n_{e,in}$	M	n_{e-ion}	ε_{extr}	$n_{e,out}$	G	$n_{ion,back}$	fraction of total IBF (sim.)	fraction of total IBF (meas.)
GEM1 (S)	1	1	14	13	0.65	9.1	9.1	3.6(28 %)	40 %	31 %
GEM2 (LP)	0.2	1.8	8	12.7	0.55	8	0.88	3.3(26 %)	37 %	34 %
GEM3 (LP)	0.25	2	53	104	0.12	12.7	1.6	1.3(1.3 %)	14 %	11 %
GEM4 (S)	1	12.7	240	3053	0.6	1830	144	0.84(0.03 %)	9 %	24 %
Total				3183		1830	1830	9(0.28 %)		

Table 3.5: Comparison of TDR simulation and the measurements on a $10\times10\,\mathrm{cm}^2$ prototype [13].

The TDR simulation is repeated in the thesis to compare the transport parameters. The voltage setting used in the thesis simulation is same as TDR simulation voltage setting. As the exact information about the setup of the TDR simulation such as penning transfer probability is not available, 85 % penning transfer probability is applied in the thesis simulation. In Fig. 3.14a, it can be seen that $\varepsilon_{coll,e}$ is the same. A noticeable difference between the $\varepsilon_{ext,e}$'s for GEM1 and GEM2 can be seen in Fig. 3.14b. A probable reason might be that the definitions of $\varepsilon_{ext,e}$ are different. The Effective gains are comparable in the case of GEM2 and GEM3. In the case of GEM1 and GEM4, the thesis simulation produces lower effective gain than that of TDR simulation because of the lower $\varepsilon_{ext,e}$. As a result, the total effective gain for the thesis simulation is much lower (881) than the TDR simulation (1830). The multiplication values (Fig. 3.14c) are also similar except for GEM2. In the case of TDR, it goes down from GEM1 to GEM2, although the GEM voltage increases from GEM1 to GEM2. The thesis simulation does not reproduce the similar trend. Instead, it shows an increase in multiplication from GEM1 to GEM2 as $\Delta\mathrm{U}_G$ increases. The definition of multiplication in the TDR simulation obtained from [24] is:

$$\mathrm{M} = \frac{\text{Number of total produced electron} - \text{Number of electron absorbed by the Kapton}}{\text{Number of incoming electron}}$$

It can be seen that the thesis definition of multiplication given in (3.3) is different than the TDR one. It can be a possible reason for different results.

As the exact penning transfer probability used in the TDR simulation is unknown, a coarse scan through the penning transfer probability is carried out for effective gain and multiplication. The idea was to see if the simulation results can get closer to the TDR simulation results. The scan would help infer the penning transfer probability as well. The 'Star Points' are the values of the corresponding GEMs from the TDR simulation (see Fig. 3.15 and 3.16). They are positioned at the point along the X-axis where the penning transfer is 85 % because the thesis simulation is done with the same penning transfer probability. Figure 3.15 shows that effective gain for GEM2 GEM3 and GEM4 get closer to the TDR simulation at 85 % penning transfer probability. For GEM1, effective gain of the thesis simulation is quite lower than that of TDR simulation. In the case of multiplication, it matches with the TDR values for GEM3 and GEM4 at 85 % penning transfer probability. For GEM1 and GEM2, multiplication values are significantly different. The collection and the extraction efficiencies of electron remained unchanged through the whole penning transfer probability range.

Finally, the calculations for the 4-GEM stack by using the transport parameters for each GEM are also done for the thesis simulation and compared with the TDR simulation's 4-GEM stack results (see Table 3.6). It is clear that because of having less than half the total effective gain in the simulation than that of TDR simulation, the IBF is relatively high.
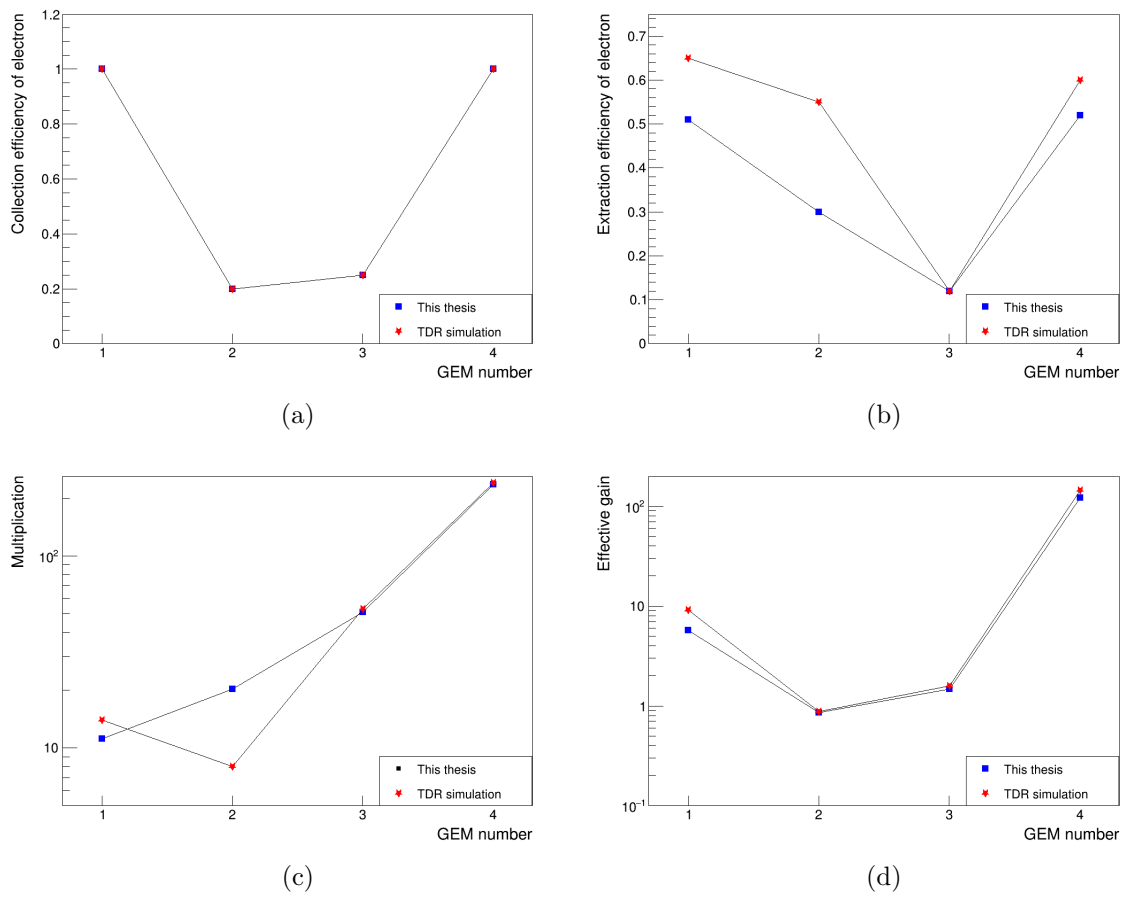
(a)

(b)

(c)

(d)

Figure 3.14: Comparison between the transport parameters shown in [13] and the values taken from the thesis simulation using the same voltage setting.
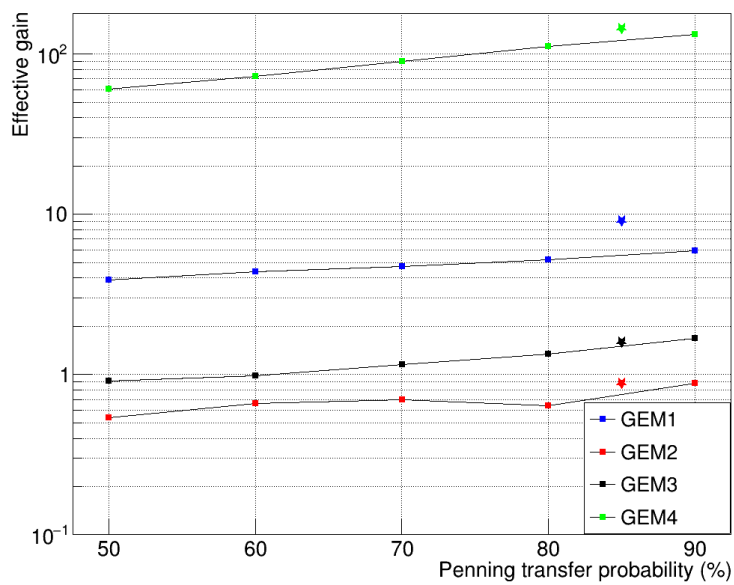

Figure 3.15: A scan of effective gain through the penning transfer probability range.
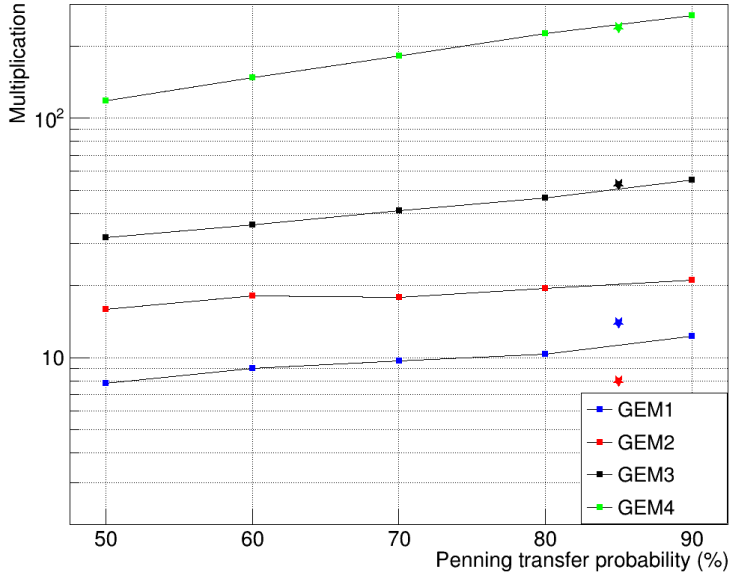
Figure 3.16: A scan of multiplication through the penning transfer probability range.

	TDR simulation	This thesis
Total effective gain	1830	881
IBF	0.5 %	1.2 %
Epsilon	9	9.2

Table 3.6: Comparison of the total effective gain, IBF and the epsilon value between the TDR simulation and the thesis simulation.

3.6 Comparison with a dedicated IBF measurement

In a dedicated IBF measurement [20], the motion of the ions through GEM foils with different ΔU_Gs and E_Ts was investigated. IBF for the 4-GEM stack was also measured by measuring the current produced by back drifting ions and the electrons. The voltage setting used for that measurement is mentioned in Table 2.1. From that IBF measurement, information about several transport parameters is collected. A simulation is carried out with the same voltage setting used in the IBF measurement. The simulation is done with 85 % penning transfer probability. The data are comparable to the previous experiment. Fig. 3.17a shows that the collection efficiency and the extraction efficiency trends are similar in *ion transport* process. A slight difference in GEM1's extraction efficiency values can be seen in Fig. 3.17b. As a result, a slight difference in transfer efficiencies of GEM1 can be seen in Fig. 3.17c. The extraction efficiencies of ions from the *avalanche* process are comparable (see Fig. 3.17d). However, the total IBF produced by the simulation is significantly higher (2 %) than the IBF of the measurement (0.57 %).
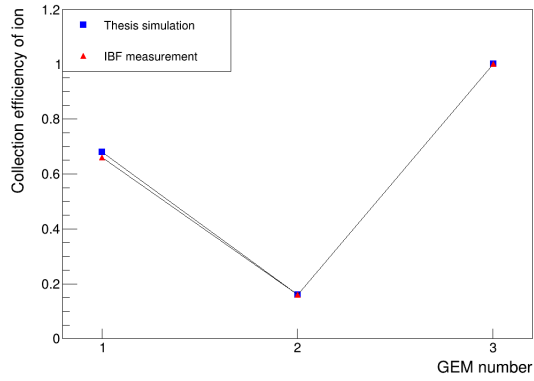
(a) Collection efficiency of ions.
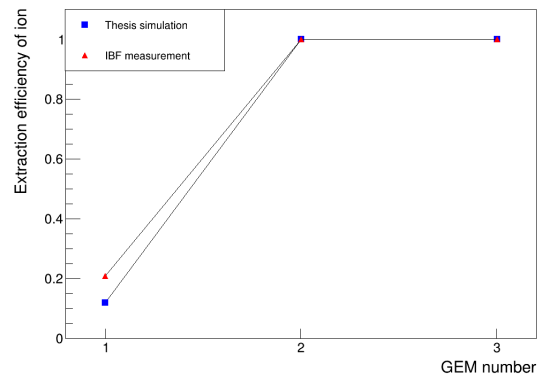
(b) Extraction efficiency of ions.
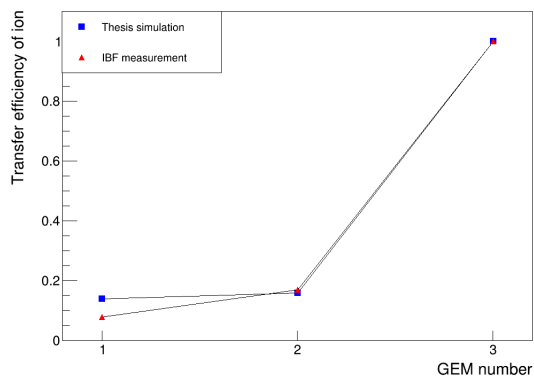
(c) Transfer efficiency of ions.
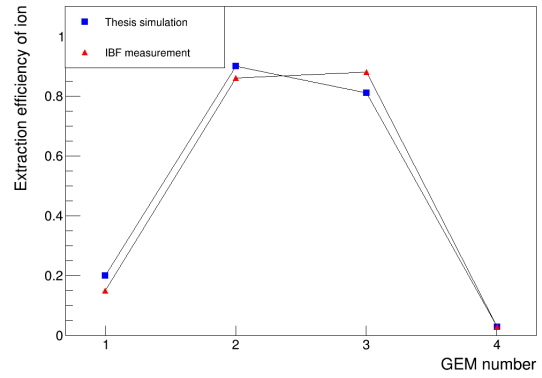
(d) Extraction efficiency of ions (*avalanche* process).

Figure 3.17: Comparison between an IBF measurement and the thesis simulation. (a),(b) and (c) represents the *ion transport* process. Graphics (d) shows the extraction efficiency of ion in the *avalanche* process.

3.7 The impact of adding a rim

A study was done to investigate the impact of adding a rim to the copper surface (see Fig. 3.18). As discussed in Section 1.5, the GEM holes have an outer and inner diameter because of their double conical shape. The outer diameter is the diameter measured between the edge of the metal layer. It means that the edges of the Kapton and the Copper end at the same point.
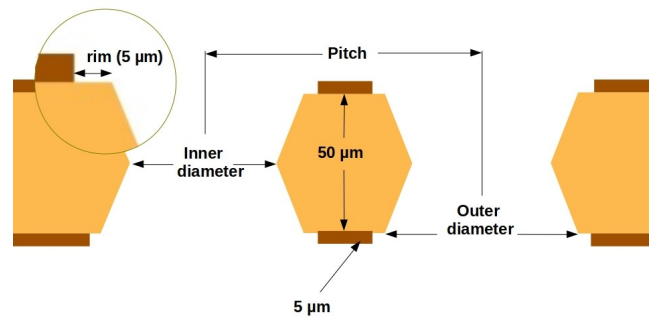
Figure 3.18: A 2D view of GEM holes that has rim in its geometry.

31

In the case of a rim, the edges of the Copper and the Kapton are not aligned. The edge of the metal surface ends slightly before the edge of the Kapton. It can happen because of over-etching. Therefore, this new geometric parameter called rim is created. It is defined as the distance between the border of the outer diameter and the metal layer's border. The influence of a rim of 5 μm was studied. Therefore, the outer diameter of the Kapton is 10 μm shorter than the metal to metal diameter.

After including the rim in the GEM geometry, a simulation was carried out to analyze its effect on electron and ion movement through the 4-GEM stack. The voltage setting 'B' and Ne-CO$_2$-N$_2$ (90-10-5) gas mixture were used for the simulation. The process is the same as what is done in Section 3.3 for the GEMs without a rim.

The addition of a rim has a significant effect on the electron amplification process. The first observation is that the field lines become less focused inside the hole. Thus, the field line density decreases, which causes less electron-ion production. A comparison of the field lines with and without rim is shown in Fig. 3.19 for GEM1 and GEM4. Graphics for GEM2 and GEM3 can be found at Fig. B.1 in the Appendix.

(a) GEM1 without rim.

(b) GEM1 with rim.

(c) GEM4 without rim.

(d) GEM4 with rim.
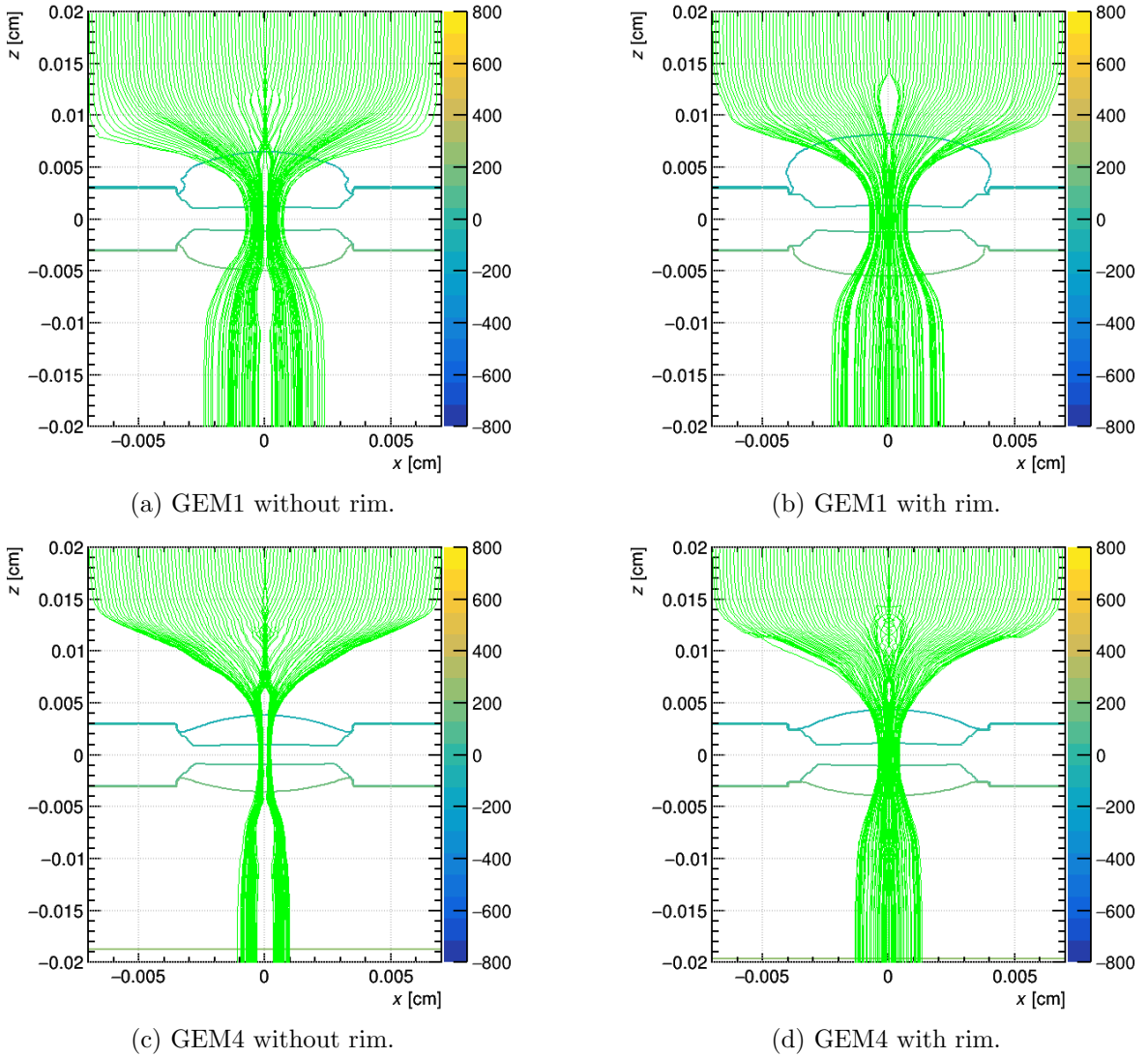
Figure 3.19: A comparison between the electric field line densities for GEM with rim and without rim. The colored bar on the right side of each plot indicates the change of potential.

Secondly, as the electron-ion production changes for including a rim to the GEM, the

other parameters also change. The only change made in the simulation setup is the addition of a rim to the GEM geometry.
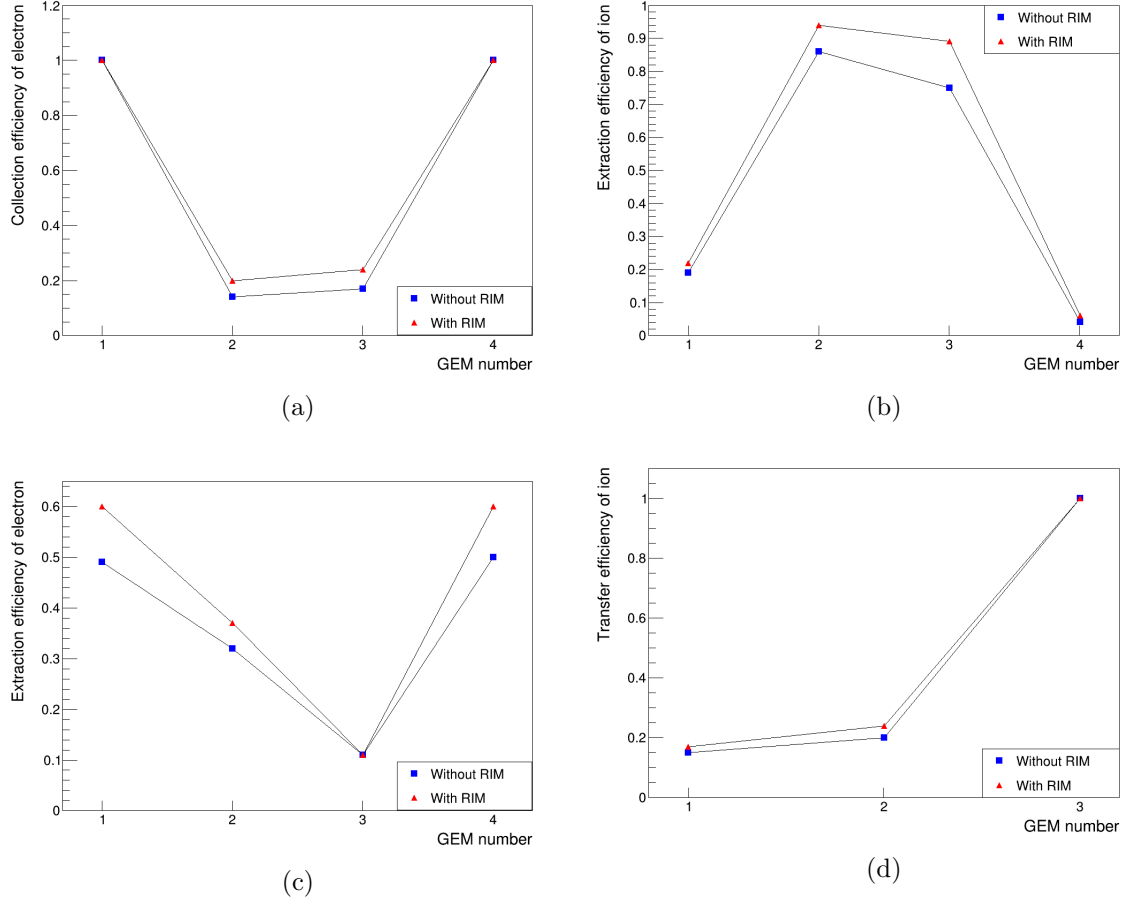
Figure 3.20: Comparison between the transport parameters with rim and without rim.

In Fig. 3.20c and 3.20a, we can see that the $\varepsilon_{coll,e}$ and $\varepsilon_{ext,i}$ get higher because of including a rim, especially in the case of GEM2 and GEM3.
However, $\varepsilon_{tr,i}$, related to the *ion transport* process, does not experience significant changes (see Fig. 3.20d). Effective gain and multiplication also shows a downward trend (see Fig. 3.21a and 3.21b) as they directly depend on the electron-ion production rate by their definition.
Data accumulated from these two separate simulations are used in the formula to calculate the results for the 4-GEM stack. Table 3.7 shows that adding a rim to the GEM causes the total effective gain to decrease and the IBF to increase.

	Without rim	With rim
Total effective gain	786.5	433.15
IBF	2.2 %	3 %
Epsilon	16	12.5

Table 3.7: A comparison between two sets of 4-GEM stacks with and without rim for voltage setting 'B'.
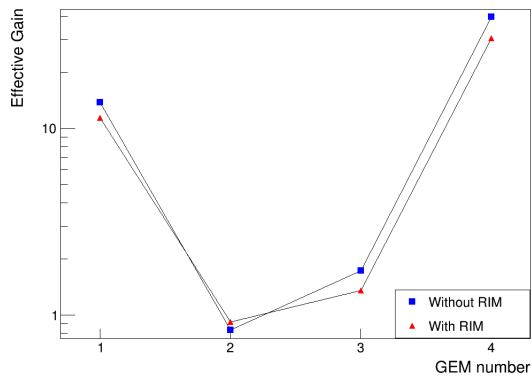
(a)
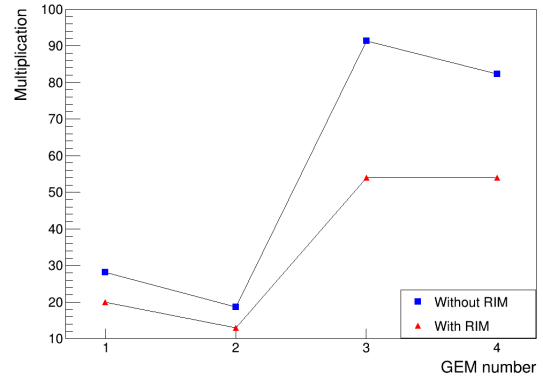
(b)
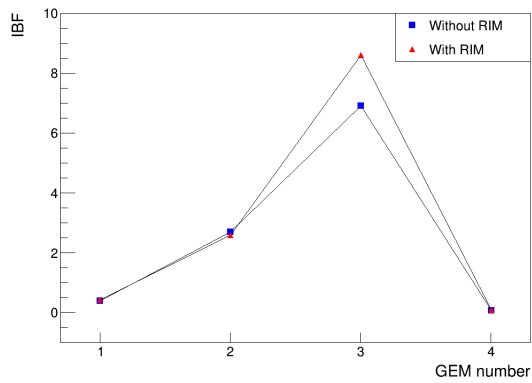
(c)
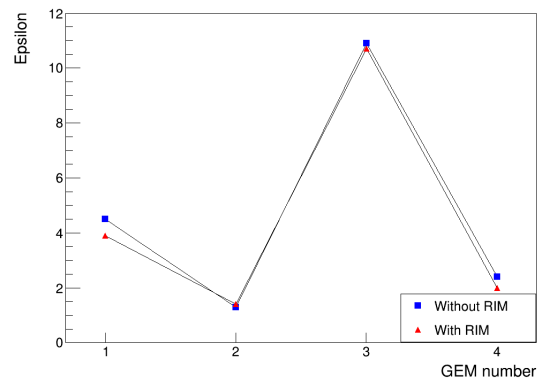
(d)

Figure 3.21: Comparison between the transport parameters with rim and without rim.

Chapter 4

Limitations of the simulation

As can be seen in Section 3.3 the simulation does not reproduce the results of the prototype measurements. Some reasons that can be responsible for that mismatch are discussed in this chapter.

It is well observed that the alignment-misalignment of the GEM foils has a great effect on the back drifting ions. In Section 2.4, it is described that in a quadruple GEM setup, the 90° rotation of adjacent GEM foils does a randomization on average. Thus, a randomized distribution of the starting points of ions and electrons for single GEM simulation is used. In the case of 90° rotation, the position of the GEM holes are changed but in this single GEM simulation the position of the ions are changed. It might be possible that changing the position of input ions does not recreate the exact environment for ions as 90° rotation does.

(a) GEM1   (b) GEM4
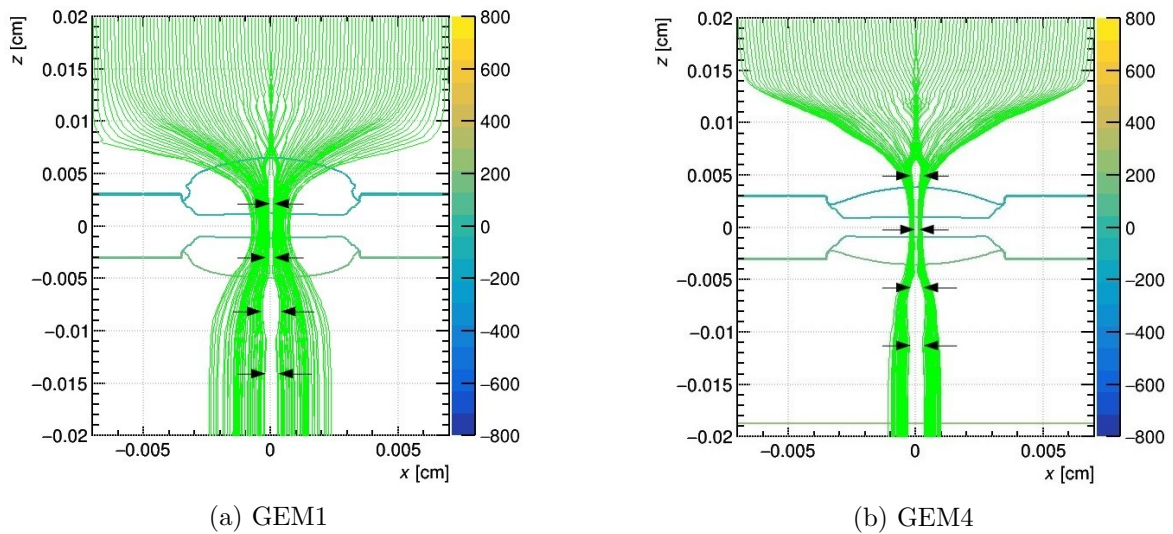
Figure 4.1: Field lines for GEM1 and GEM4 produced by Garfield++. Absence of field line can be seen through the center of the GEM hole.

An unexpected feature can be spotted in the visualization of the field lines produced by the simulation. Especially for GEM1 and GEM4, it shows no field lines at some points of the exact middle of the GEM hole along the Z-axis (see Fig. 4.1). It was not further investigated whether it is an error of ANSYS that calculates the potentials or just a visualization problem of Garfield++. The former one would effect the avalanche significantly as the highest electron-ion production occurs in the middle of the GEM. This problem might be connected to the pitch length as they are observed mainly in GEM1 and GEM4 that have the same pitch length (140 µm). For GEM3 and GEM4, this error fades away from the graphics (see Fig. B.1).

Another technical limitation lies in 'Garfield++' itself. It systematically underestimates the effective gain. The reason is that the path of an electron between two collisions is always considered as a straight line. However, it can be said that the path is influenced because electron moves under a strong electric field inside a GEM hole. Therefore, it can be assumed that the path length of electron inside the GEM hole is underestimated which results in a reduced number of interaction. As a result, the simulation yields lower number of electron-ion production which gives low effective gain [25, p. 95].

The attachment rate of electrons is not taken care of precisely. Although it can be seen in Table 3.2 that the attachment contributions are quite small and including them to the $\varepsilon_{ext,e}$ and G_{eff} calculation do not help obtaining the Total Effective Gain closer to 2000. In fact, it does the opposite.
The drift gap and the induction gap in the simulation are only 1 mm that is smaller than the real setup. Thus, more electrons will get attached as they will travel more distance. As a result, the $\varepsilon_{ext,e}$ and G_{eff} will be different.

Chapter 5

Summary

A significant part of the ALICE TPC upgrade was to replace the MWPC with new GEM-based technology. Unlike MWPC, it will provide a non-gated continuous operation which allows the TPC to overcome its rate limitation.

In order to understand the movements of electrons and ions through a GEM foil, a simulation is carried out in this thesis. As the proposed baseline quadruple GEM stack configuration is S-LP-LP-S, the simulation is also done with standard (S) and large pitch (LP) GEMs. The simulation is done for each GEM foil separately. Ne-CO_2-N_2 (90-10-5) gas mixture is used, and the so-called voltage setting 'B', which optimizes operational stability, is used for the simulation. Various transport parameters are defined, and formulas are formed to calculate the total effective gain, IBF, and epsilon. The extracted data from the simulation is used to see the trend of the transport parameters for each GEM.

The changing patterns of the transport parameters are analyzed. The factors that contribute to their change are the applied field above and below a GEM, the potential difference between the top and bottom electrodes of a GEM, and the pitch length of GEM. The effects of these parameters are described in detail. The efficiency of the primary electron entering the GEM hole gets higher when the field above the GEM gets lower. The production of electron-ion pairs increases with the increase of GEM voltage. The extraction efficiency of the electron is high if there is a high field below the GEM. The higher field above the GEM helps more ions to escape the GEM.

It can be said that the changing pattern of the transport parameters and the reasons for the change is well understood. However, the combined results for the 4-GEM stack are unable to match with the previous measurements and simulations. The probable reasons behind this difference are also described.

The effects of penning transfer probability and including a rim to the GEM geometry are also described. The production of electron-ion pairs increases with the increase of penning transfer probability. GEMs without a rim produce a larger avalanche which leads to higher effective gain.

Instead of a single GEM simulation, a 4-GEM stack simulation can be the immediate next step to continue further research. Moreover, further research can be done with different rim lengths or rim on the one side of a GEM electrode while no rim on the other side. The effect of changing the gap between two neighboring GEMs is also a potential topic to investigate.

Acknowledgments

First and foremost, I would like to express my sincere gratitude to my supervisor, Professor Dr. Harald Appelshäuser, for giving me the chance to do my thesis in his group. I also want to thank him for his incredible support during my thesis. I am grateful to work under his supervision. Secondly, I would like to thank Dr. Jens Wiechula, the second examiner of this thesis and my mentor, for his invaluable advice, continuous supports, and patience. Without his vast knowledge, motivation, and tremendous understanding, it would have been impossible for me to complete the thesis.

A large part of the credit for my successful completion goes to the 'Sandvoss Stipendium'. I have received a scholarship from them during my thesis period. Without their support, I would not be able to continue my study. I want to express my heartiest respect to Mrs. Sandvoss for her extraordinary contribution to my life. I also want to thank professor Dr. Marc Wagner, who helped me get the scholarship and guided me to find the right group for the thesis. He also motivated me to work hard during my thesis.

I want to thank all the group members for sharing their knowledge and making a friendly environment. Specially, Janik Ditzel, Christoph Weidlich, Michael Hartung and Fabian Liebske for their support.

Sebastian Scheid, Michael Jung also helped with their previous experience and expertise. I am also grateful to them.

I want to thank Taku Gunji, associate professor of CNS, university of Tokyo and Chilo Garabatos from GSI for sharing their opinion and experience.

I thank my mother Nurjahan Begum for being patient and having faith in me in the most challenging time. I also thank my uncles, Moin Uddin, Foiz Ahmed and Shuaive Ahmed, for their endless support throughout my student life. Without their backup, I would not be able to dream about studying in this prestigious university in the first place.

I am also thankful to my boss at work, Gabriele Rämsch, and other colleagues to help me adjust my work and study schedule and motivate me.

I want to dedicate this thesis to my late father Saif Uddin Ahmed, who would have been the proudest person for my achievement.

Appendices

Appendix A

Endpoints of the electrons and ions

In section Section 3.2, graphics of the endpoints of the electrons and ions for GEM1 were displayed. In this chapter similar graphics for GEM2, GEM3 and GEM4 are also shown. Electron and ion endpoints along the Z-axis and according to their status code for GEM2, GEM3 and GEM4 are presented in Fig. A.1, A.2 and A.3. Figure A.4 displays the endpoints of the ions in the *ion transport* process.
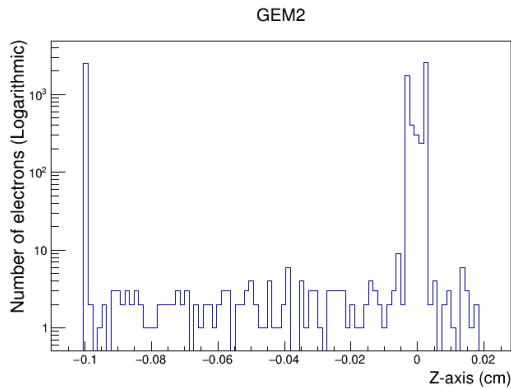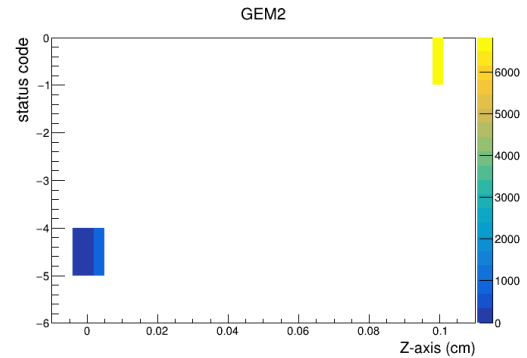

(a) Electron endpoints.
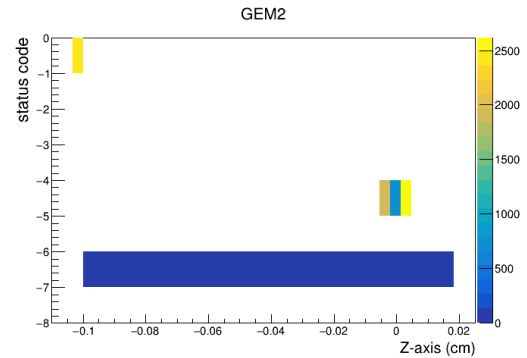
(b) Electron endpoints according to their corresponding status code.
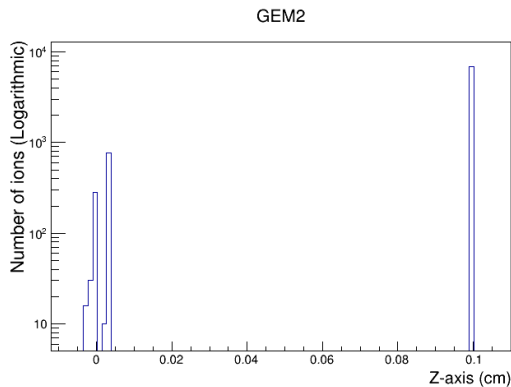
(c) Ion endpoints.

(d) Ion endpoints according to their corresponding status code.

Figure A.1: End points of the electrons and ions created in the *avalanche* process in GEM2. The colored bar on the right side shows the number of electrons.
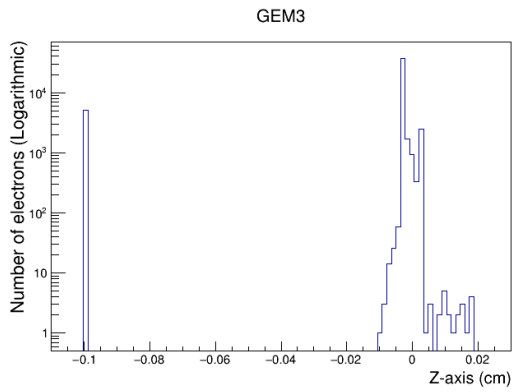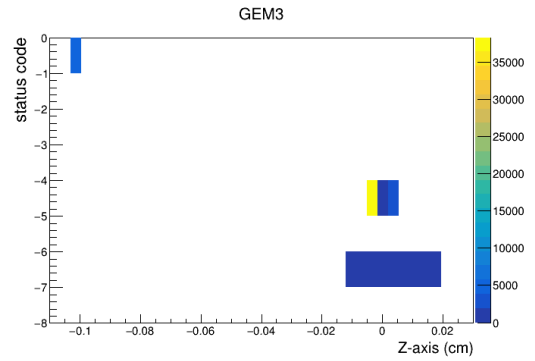
(a) Electron endpoints.

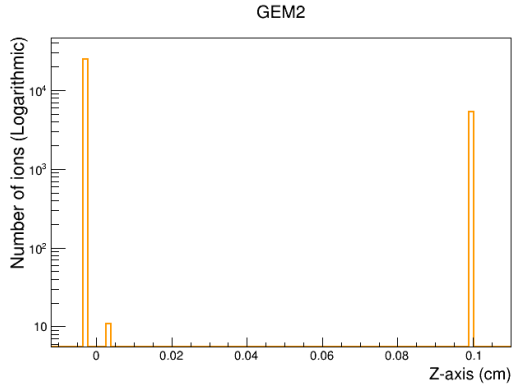(b) Electron endpoints according to their corresponding status code.
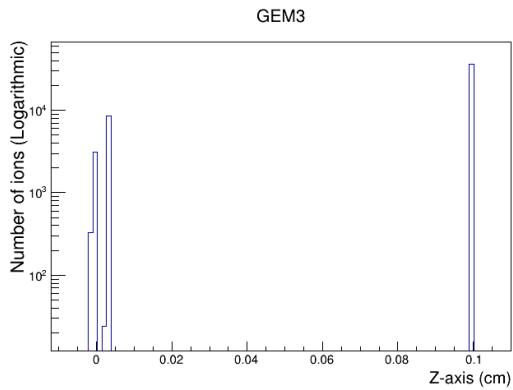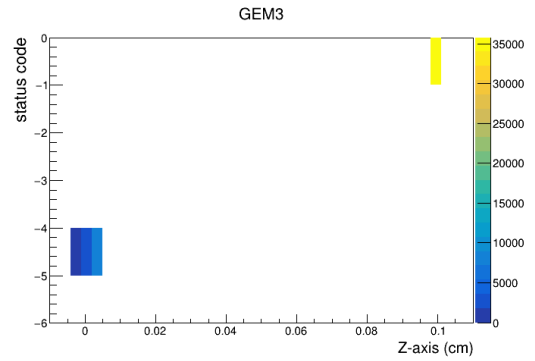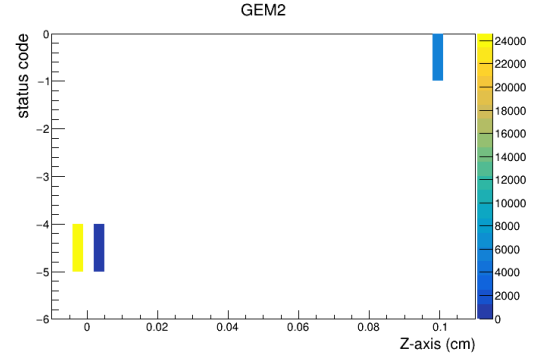

(c) Ion endpoints.

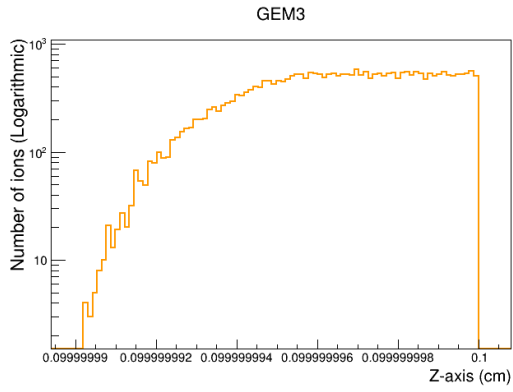(d) Ion endpoints according to their corresponding status code.

Figure A.2: Endpoints of the electrons created in the *avalanche* process in GEM3. The colored bar on the right side shows the number of electrons.
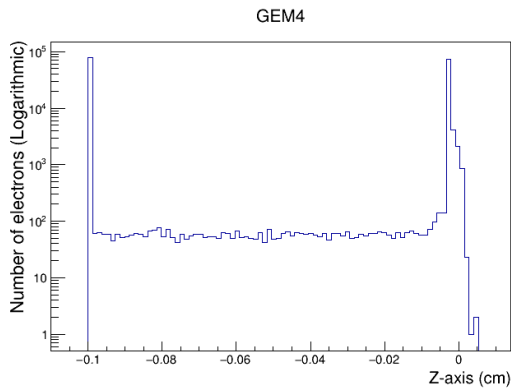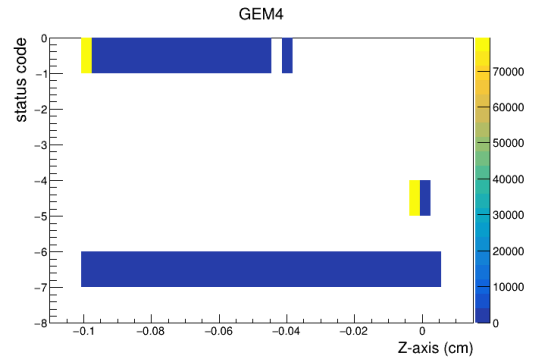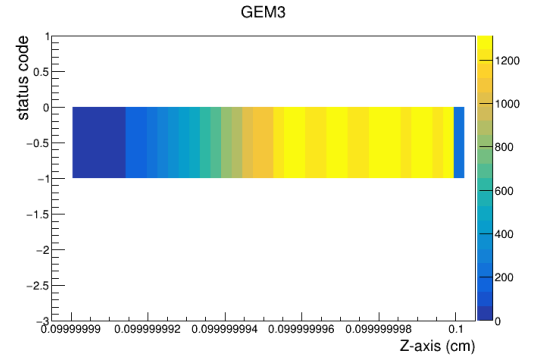
(a) Electron endpoints.

(b) Electron endpoints according to their corresponding status code.
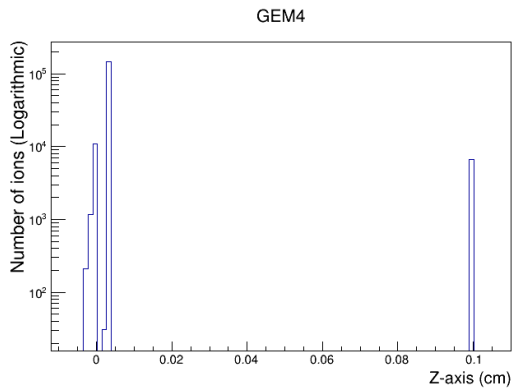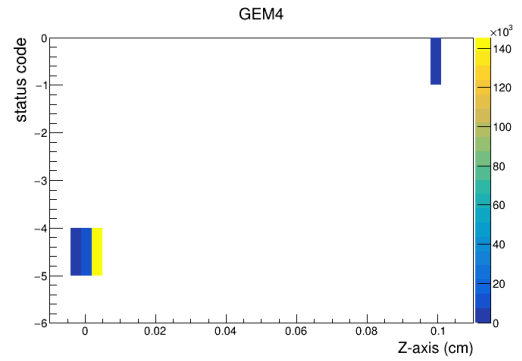
(c) Ion endpoints.

(d) Ion endpoints according to their corresponding status code.

Figure A.3: End points of the electrons created in the *avalanche* process in GEM4. The colored bar on the right side shows the number of electrons.
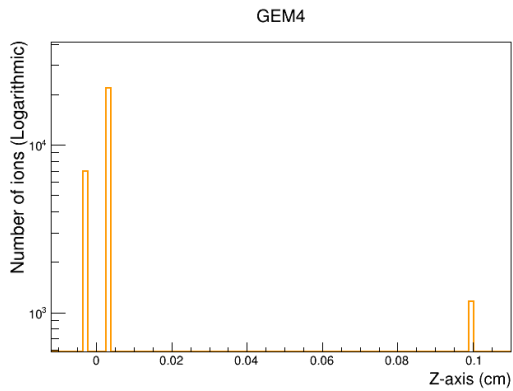
(a) Ion endpoints.

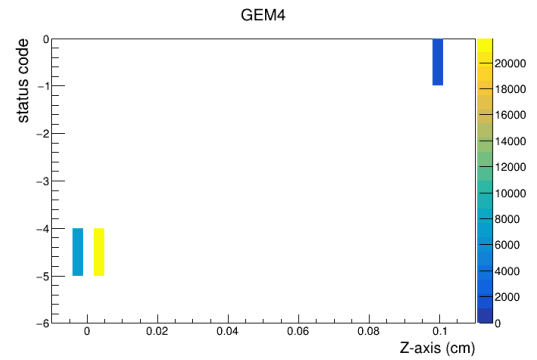(b) Ion endpoints according to their corresponding status code.

(c) Ion endpoints.

(d) Ion endpoints according to their corresponding status code.

(e) Ion endpoints.

(f) Ion endpoints according to their corresponding status code.

Figure A.4: Endpoints of the ions coming from another GEM (*ion transport* process) for GEM2, GEM3 and GEM4. The colored bar on the right side shows the number of ions.

Appendix B

Simulation data

The transport parameters obtained from the simulation for voltage setting 'B' is presented in Table B.1.

	Avalanche process				*Ion Transport* process			
	GEM1	GEM2	GEM3	GEM4	GEM1	GEM2	GEM3	GEM4
$\varepsilon_{coll,i}$					0.7	0.2	1	0.77
$\varepsilon_{ext,i}$	0.19	0.86	0.75	0.041	0.22	1	1	0.051
$\varepsilon_{tr,i}$					0.15	0.2	1	0.039
$\varepsilon_{ext,e}$	0.5	0.32	0.11	0.5				
$\varepsilon_{coll,e}$	1	0.14	0.17	1				
M	28.2	18.64	91.32	82.3				
G_{eff}	13.8	0.83	1.73	39.7				
IBF	0.4	2.7	6.9	0.08				
ϵ	4.5	1.3	10.9	2.4				

Table B.1: The transport parameters calculated from the simulation with voltage setting 'B'.

Table B.2 and B.3 show the effective gain, multiplication, IBF, and epsilon data calculated in the penning transfer probability scan for voltage setting 'B'. Table B.4 contains the trends transport parameter data for 4-GEM stack with their corresponding penning transfer probability. In Table B.5, data produced from the thesis simulation done with the TDR voltage setting and the actual TDR simulation is presented.

Penning Transfer Probability (%)	Effective gain				Multiplication			
	GEM1	GEM2	GEM3	GEM4	GEM1	GEM2	GEM3	GEM4
25	5.8	0.5	0.61	14.52	12.1	12	34.8	29.9
35	6.8	0.5	0.73	17.04	14	13.2	40.02	34.8
45	7.7	0.6	0.92	20.34	16	13.6	47.9	41.6
55	9.3	0.6	0.97	23.8	19	15	53.6	48.2
65	10.4	0.74	1.18	28.51	20.9	16	62.9	57.6
75	12.04	0.84	1.37	32.4	24.7	17.1	72	65.5
85	13.5	0.79	1.69	39.4	27.5	17.5	84.1	79.6
95	15.7	1.02	1.84	46.4	31.3	20.6	97.2	92.9

Table B.2: Data from the penning transfer probability scan for Effective gain and Multiplication with voltage setting 'B'.

Penning Transfer Probability (%)	IBF				Epsilon			
	GEM1	GEM2	GEM3	GEM4	GEM1	GEM2	GEM3	GEM4
25	0.52	3.6	8.02	0.13	1.99	0.7	3.9	0.95
35	0.49	3.62	7.4	0.13	2.4	0.7	4.7	1.1
45	0.48	3.34	7.3	0.11	2.7	0.83	5.7	1.3
55	0.45	3.2	7.22	0.12	3.2	0.93	6	1.54
65	0.43	3.03	7.2	0.096	3.6	1.03	7.5	1.8
75	0.43	2.7	7.12	0.094	4.14	1.3	8.8	2.05
85	0.41	2.8	7	0.087	4.6	1.2	10.8	2.45
95	0.4	2.5	6.8	0.083	5.3	1.6	11.5	2.9

Table B.3: Data from the penning transfer probability scan for IBF and epsilon with voltage setting 'B'.

	Penning transfer probability (%)							
	25	35	45	55	65	75	85	95
G_T	25.7	42.3	79.3	131	257.7	449	750.5	1363
IBF	0.25	0.17	0.1	0.073	0.048	0.033	0.023	0.017
Epsilon	4.95	5.9	6.9	8.5	10.5	13.9	15.8	22.1

Table B.4: Trends of total effective gain, total IBF and total epsilon with the increasing penning transfer probability.

	GEM1		GEM2		GEM3		GEM4	
	This thesis	TDR sim.	This thesis	TDR sim.	This thesis	TDR sim.	This thesis	TDR sim.
$\varepsilon_{ext,e}$	0.51	0.65	0.3	0.55	0.12	0.12	0.6	0.52
$\varepsilon_{coll,e}$	1	1	0.2	0.2	0.25	0.25	1	1
M	11.2	14	20.3	8	51.1	53	235.3	240
G_{eff}	5.7	9.1	0.86	0.88	1.48	1.59	121.5	144

Table B.5: Comparison between the data produced by repeating the TDR simulation and the actual TDR simulation data.

		GEM1		GEM2		GEM3		GEM4	
		This thesis	IBF meas:	This thesis	IBF meas:	This thesis	IBF meas:	This thesis	IBF meas:
Ion transport process	$\varepsilon_{coll,i}$	0.66	0.68	0.16	0.16	1	1		
	$\varepsilon_{ext,i}$	0.12	0.21	1	1	1	1		
Avalanche process	$\varepsilon_{ext,i}$	0.2	0.15	0.9	0.86	0.81	0.88	0.03	0.03

Table B.6: Comparison between the thesis data and the IBF measurement.

B.1 Data from the GEM with rim

Figure B.7 shows the data collected from the simulation of each GEM foil that has rim in its geometry. The comparison with the transport properties of GEMs without rim is described in Chapter 3.7. In Fig. B.1, it can be seen that the field line density inside the GEM hole changes because of the addition of rim.
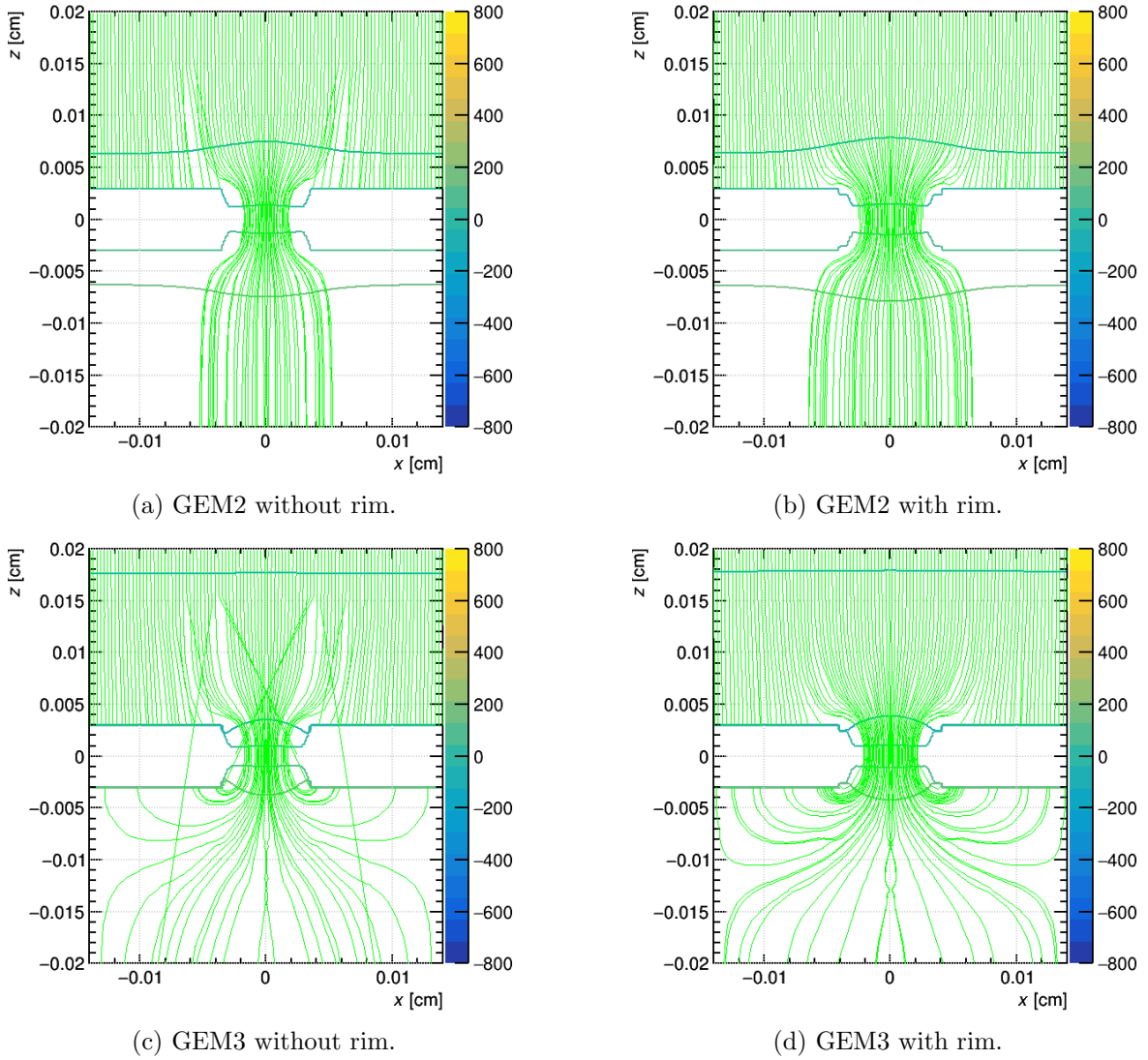

(a) GEM2 without rim.

(b) GEM2 with rim.

(c) GEM3 without rim.

(d) GEM3 with rim.

Figure B.1: A comparison between the electric field line densities in the case of GEM without rim and GEM with rim. The colored bar on the right side of each plot indicates the change of potential.

	Avalanche process				Ion Transport process			
	GEM1	GEM2	GEM3	GEM4	GEM1	GEM2	GEM3	GEM4
$\varepsilon_{coll,i}$					0.7	0.2	1	0.77
$\varepsilon_{ext,i}$	0.24	0.94	0.89	0.06	0.22	1	1	0.051
$\varepsilon_{tr,i}$					0.15	0.2	1	0.039
$\varepsilon_{ext,e}$	0.6	0.37	0.11	0.6				
$\varepsilon_{coll,e}$	1	0.2	0.24	1				
M	20	13	53.96	54				
G_{eff}	11.4	0.92	1.36	30.5				
IBF	0.43	2.6	8.6	0.1				
ϵ	3.9	1.4	10.7	2				

Table B.7: The transport parameters calculated from the simulation with voltage setting 'B' where rim is included to the GEM geometry.

List of Figures

List of Tables

List of References

[1] K. Aamodt et al. The ALICE experiment at the CERN LHC, 2008.

[2] The ALICE Collaboration, K Aamodt, A Abrahantes Quintana, R Achenbach, et al. The ALICE experiment at the CERN LHC. *JINST*, 3(08):S08002–S08002, aug 2008.

[3] Antonin Maire and David Dobrigkeit Chinellato. ALICE sub-detectors highlighted. https://cds.cern.ch/record/2302924, May 2017. General Photo.

[4] J Adolfsson, M Ahmed, S Aiola, J Alme, T Alt, W Amend, F Anastasopoulos, C Andrei, M Angelsmark, V Anguelov, et al. The upgrade of the ALICE TPC with GEMs and continuous readout. *JINST*, 16(03):P03022, 2021.

[5] Jens Wiechula. *Commissioning and Calibration of the ALICE-TPC*. PhD thesis, Institut für Kernphysik, Goethe universität, 2008.

[6] Ernst Hellbär. Ion Movement and Space-charge Distortions in the ALICE TPC. Master's thesis, Institut für Kernphysik, Goethe universität, 2015.

[7] Rob Veenhof. Choosing a gas mixture for the ALICE TPC. *ALICE internal note*, page 160, 2003.

[8] The ALICE Collaboration. Upgrade of the ALICE Time Projection Chamber. http://cds.cern.ch/record/1622286, 2013.

[9] Fabio Sauli. GEM: A new concept for electron amplification in gas detectors. *Nuclear Instruments and Methods in Physics Research Section A: Accelerators, Spectrometers, Detectors and Associated Equipment*, 386(2-3):531–534, 1997.

[10] A. T. Perez Fontenla. Scanning Electron Microscopy (SEM) and Focus Ion Beam (FIB) analysis on heavily irradiated gas electron multipliers (GEMs)-Document 1719614 (v.1). https://edms.cern.ch/ui/#!master/navigator/document?D:1173329344:1173329344:subDocs, 2016.

[11] Marco Villa, Serge Duarte Pinto, Matteo Alfonsi, Ian Brock, Gabriele Croci, Eric David, Rui De Oliveira, Leszek Ropelewski, Hans Taureg, and Miranda van Stenis. Progress on large area GEMs. *Nuclear Instruments and Methods in Physics Research Section A: Accelerators, Spectrometers, Detectors and Associated Equipment*, 628(1):182–186, 2011.

[12] The upgrade of the largest gas detector in the world: the ALICE GEM-TPC project. https://www.groups.ph.tum.de/denseandstrange/research/current-projects/gem-tpc-upgrade-project-at-alice/. (Accessed on 04/09/2021).

[13] The ALICE Collaboration. Addendum to the Technical Design Report for the Upgrade of the ALICE Time Projection Chamber. https://cds.cern.ch/record/1984329/files/, 2015.

[14] H Schindler. Garfield++ user guide. `https://garfieldpp.web.cern.ch/garfieldpp/documentation/UserGuide.pdf`. (Accessed on 02/08/2021).

[15] O Bouianov, M Bouianov, R Orava, P Semenov, and V Tikhonov. Progress in gem simulation. *Nuclear Instruments and Methods in Physics Research Section A: Accelerators, Spectrometers, Detectors and Associated Equipment*, 450(2-3):277–287, 2000.

[16] Stephen Biagi. Transport of electrons in gas mixtures. `https://magboltz.web.cern.ch/magboltz/`. (Accessed on 02/01/2021).

[17] SF Biagi. Monte Carlo simulation of electron drift and diffusion in counting gases under the influence of electric and magnetic fields. *Nuclear Instruments and Methods in Physics Research Section A: Accelerators, Spectrometers, Detectors and Associated Equipment*, 421(1-2):234–240, 1999.

[18] ROOT - All Reference Guides. `https://root.cern/reference/`. (Accessed on 12/01/2020).

[19] Ansys - engineering simulation software. `https://www.ansys.com/`. (Accessed on 04/08/2021).

[20] Fabian Liebske. Direkte Messung der Ionenbewegung druch eine mehrlagige GEM-Anordnung. Master's thesis, Institut für Kernphysik, Goethe universität, 2020.

[21] Goethe Universität, Institut für Kernphysik. `https://www.uni-frankfurt.de/45141900/Institut_f%C3%BCr_Kernphysik`. (Accessed on 03/25/2021).

[22] Ö Šahin, T.Z. Kowalski, and R. Veenhof. Systematic gas gain measurements and Penning energy transfer rates in Ne - CO2 mixtures. *JINST*, 11(01):P01003–P01003, 2016.

[23] Sebastian Excitation Levels of Neon-OpenWetWare. `https://openwetware.org/wiki/Sebastian_Excitation_Levels_of_Neon#:~:text=The%20accepted%20values%20for%20the,19.75%20eV`. (Accessed on 04/08/2021).

[24] T. Gunji. Private communication.

[25] Jonathan Ottnad. *Optimierung der GEM-basierten Verstärkungsstufe einer TPC für das CB/TAPS-Experiment*. PhD thesis, U. Bonn (main), 2020.

Eigenständigkeitserklärung

Hiermit erkläre ich, dass ich die Masterarbeit selbstständig und ohne Benutzung anderer als der angegebenen Quellen und Hilfsmittel verfasst habe. Alle Stellen der Arbeit, die wörtlich oder sinngemäß aus Veröffentlichungen oder aus anderen fremden Texten entnommen wurden, sind von mir als solche kenntlich gemacht worden. Ferner erkläre ich, dass die Arbeit nicht -auch nicht auszugsweise- für eine andere Prüfung verwendet wurde.

Frankfurt am Main, April. 2021   Misbah Uddin Ahmed